Quantification of the Land Surface and Brown Ocean Influence on Tropical Cyclone Intensification Over Land

Jinwoong Yoo[1], Joseph A. Santanello, Jr.[2], Marshall Shepherd[3], Sujay Kumar[2], Patricia Lawston[1], and Andrew M. Thomas[3]

1 University of Maryland (ESSIC)/NASA Goddard Space Flight Center

2 NASA Goddard Space Flight Center

3 University of Georgia

Corresponding Author: Dr. Jinwoong Yoo

NASA-GSFC, Code 617, Bldg. 33, Room G207, Greenbelt, MD 20771 USA

Jinwoong.yoo@nasa.gov

Revision Submitted to *Journal of Hydrometeorology*

Abstract

An investigation of TC Kelvin in February 2018 over northeast Australia was conducted to understand the mechanisms of the Brown Ocean effect (BOE), and to develop a comprehensive analysis framework for landfalling tropical cyclones (TCs) in the process. NASA's Land Information System (LIS) coupled to the NASA Unified WRF (NU-WRF) system was employed as the numerical model framework for 12 land/soil moisture perturbation experiments. Impacts of soil moisture and surface enthalpy flux conditions on TC Kelvin were investigated by closely evaluating simulated track and intensity, midlevel atmospheric thermodynamic properties, vertical wind shear, total precipitable water (TPW), and surface moisture flux. The results suggest that there were recognized differentiations among the sensitivity simulations as a result of land surface (e.g., soil moisture and texture) conditions. However, the intensification of TC Kelvin over land was more strongly related to atmospheric moisture advection and the diurnal cycle of solar radiation (i.e., radiative cooling) than to overall soil moisture conditions or surface fluxes. The analysis framework employed here for TC Kelvin can serve as a foundation to specifically quantify the factors governing the BOE. It also demonstrates that the BOE is not a binary influence (i.e. all or nothing), but instead operates in a continuum from largely to minimally influential such that it could be utilized to help improve prediction of inland effects for all landfalling TCs.

Key words: Brown Ocean Effect, NU-WRF, LIS, soil moisture, enthalpy fluxes, TCMIs

1. Introduction

There has been an increase in attention from the scientific community, as well as the public and media, to what is referred to as the 'Brown Ocean' effect (BOE) on landfalling

tropical cyclones (TCs) (e.g., Kinghorn 2018; Emanuel *et al.* 2008). The BOE describes the ability of land surface characteristics (e.g., soil moisture and texture) to contribute to TC intensification over land, in contrast to the usual rapid decay that occurs in the majority of landfalling storms due to friction and lack of evaporative fuel from warm ocean bodies. Previous studies have highlighted the potential factors, thresholds, and conditions necessary for a BOE to be possible (e.g., Arndt *et al*. 2009; Evans *et al*. 2011; Andersen and Shepherd 2014), but much of the discussion surrounding the BOE to date remains anecdotal, ad hoc, or speculative, and there remains a lack of a robust and comprehensive analysis approach to evaluating, or quantifying, the role of the land surface in landfalling TCs. Although the definition of the BOE seems somewhat clear and the general public has started to use the term "brown ocean effect" in non-scientific conversations, the physical aspects of the characterization remain undetermined among the TC research community. Therefore, identifying and quantifying the factors and thresholds that define a brown ocean event will not only benefit public and scientific communications, but will also allow for the development of predictive capabilities for the BOE via proper simulation in coupled modeling systems.

In regard to the general environmental conditions favorable for genesis (i.e., Gray 1968, 1998), it is commonly accepted that TCs develop with three ingredients: 1) ample enthalpy in the atmospheric boundary layer created by surface latent heat fluxes from the ocean, 2) higher relative humidity in the middle troposphere, and 3) low tropospheric stability with low vertical wind shear above the warm ocean, permitting deep convections for an extended period of time beyond the general span of disturbances over the ocean (Yoo *et al.* 2016). In contrast, it is also well known that the presence of midlevel dry air and strong vertical wind shear exert a negative influence on the development of a TC (e.g., Braun *et al*. 2012; Ge *et al*. 2013).

Once developed, TCs grow into their maximum intensity and horizontal size, typically 200-2000 km, over the open ocean. In general, intensity decreases as TCs approach land due to a number of adverse environmental conditions raised by the shift of regime from ocean to land surface boundary (Kaplan and Demaria 1995; Emanuel 2000; Niyogi *et al*. 2016). Reductions in surface latent and sensible heat flux supply to the core of the storm may result in a dramatic decrease in storm's intensity. Inland heterogeneities of soil type, land use land cover, vegetation type, and topography can also play a significant role in changing the boundary layer characteristics and mesoscale processes. In most cases, these land characteristics speed up the storm's lysis process, but in some cases, they may intensify further or maintain a TCs strength inland after the storm's landfall, increasing the risk of inland inundation over the path of the TC steeply (Niyogi *et al*. 2016). For this reason, landfalling TCs and their interactions with land surface processes have gained considerable societal and scientific interest in recent years, especially from those in the local land-atmosphere coupling (LoCo) research community (Anderson and Shepherd 2014; Santanello *et al*. 2018).

When TCs intensify or maintain their strength after landfall for an extended period of time with their warm-core characteristics, this phenomenon is called a tropical cyclone maintenance or intensification event (TCMIs) (see Anderson and Shepherd (2014) and references therein). By definition, TCMIs are distinct from extratropical transition (ET) in that they retain warm-core structures similar to the TCs before landfall. TCMIs are most common over Australia despite more overall TCs originating in the western North Pacific (Andersen and Shepherd 2014). For TCMIs in northern Australia, Emanuel *et al*. (2008) argued that fresh rains over the hot sandy soils of northern Australia with a fairly high thermal diffusivity in wet condition may be responsible for the rapid surface enthalpy fluxes that can support post-landfall

storms up to marginal hurricane intensity. This preliminary work and plausible hypothesis warrant a three-dimensional, full-physics modeling study, in which heterogeneous soil temperature, moisture, and texture, can be evaluated for their contributions to the land surface fluxes of enthalpy, in an effort to further our understandings of the TCMI events.

A recent TC that exhibited TCMI and generated discussion of potential BOE influence made landfall in northern Australia in February 2018. On 17 February, a tropical low drifting southwestward intensified into an Australian Category 1 TC as confirmed by the Australian Bureau of Meteorology (BoM) offshore near the Eighty Mile Beach in northwestern Australia. Known as TC Kelvin, the storm moved eastward very slowly, then intensified quickly reaching an Australian TC Category 2 strength with the maximum sustained wind speed (wind gust) at 30 m s^{-1} (43 m s^{-1}) before its landfall at Eighty Mile Beach at 21UTC 17 February (BoM; http://www.bom.gov.au/announcements/sevwx/wa/watc20180211.shtml). Kelvin maintained its TC intensity ($\geq$ 18 m s^{-1}) after its landfall and weakened slowly over the next few days until it became a tropical low on 19 February. Before its final weakening below TC strength, multiple satellite observations suggested that Kelvin went through a secondary intensification period while inland on 19 February.

Due to these distinctive features of the TCMIs exhibited by this storm, the authors selected TC Kelvin as an initial case study for investigation into the BOE. The goals of this study are thus two-fold: 1) to establish a modeling framework with the ultimate goal of understanding and quantifying the BOE scientifically and 2) to investigate Kelvin as a case study to understand the dominant factors leading to its TCMI using state-of-the-art coupled models. It is hypothesized that the enthalpy fluxes from the land surface are the primary determinant for the post-landfall intensification of TC Kelvin, by the definition of the BOE as hypothesized by

Andersen and Shepherd (2014). The impact of the land surface conditions on the TCMI of Kelvin, which occurred over a climatological hotspot of TCMI and sandy soils in Northwest Australia, will be tested and quantified using an integrated modeling and analysis approach. We will also analyze the diurnal cycles of surface energy budgets (i.e., surface fluxes) as the storm made landfall and address the relationship between the TC intensity and the diurnal cycle over land, which has not been studied to date.

In Section 2, the modeling framework and experiment design are described. In Section 3, modeling results and analyses are presented. In Section 4, results are discussed within the context of the BOE, and conclusions follow in Section 5.

2. Data and Methods

2.1. Characterization of TC Kelvin Track and Intensity

TC Kelvin's track dataset was obtained from the Australian BoM that covers ten days of the lifecycle of TC Kelvin from 00 UTC 11 February to 21 UTC 21 February, 2018. The data went through a harmonization process to eliminate the extra-temporal observation records, yielding a 6-hourly dataset for the storm period of interest from 00 UTC 16 February to 00 UTC 20 February (see supplementary material for multiple track observation dataset comparison).

The NOAA National Centers for Environmental Information (NCEI) optimum interpolation (OI) sea surface temperature (SST) dataset (https://www.ncdc.noaa.gov/oisst/data-access; Figure 1a) suggest that warm SST favorable for TC development (> 26 °C or 299 K) was prevalent off the northern coast of Australia as well as along the intertropical convergence zone (ITCZ) near the equator. This implies that high ocean heat energy stored along the coast of

115 northwestern Australia satisfied one of the key requirements for a pre-existing vortex to
116 intensify.

117 The NASA Moderate-resolution Imaging Spectroradiometers (MODIS) image on 19
118 February (Fig. 1b) clearly depicts the zonal placement of the ITCZ to the north of Australia and
119 the post-landfall of Kelvin in the northwestern Australia maintaining its TC structure as well as
120 eyewall inland, approximately 32 hours after landfall. The inner radius of the eyewall was
121 estimated to be about 20 km at that time and the center of the storm was about 340 km away
122 from the nearest coast. Rainbands are clearly visible both south and north of the eye, which
123 suggests that the storm was not yet affected by midlatitude systems at that time.

124 2.2. Coupled Modeling Framework

125 The integrated modeling approach using the three-dimensional, full-physics model is
126 beneficial for TCMI investigations because the land-atmosphere coupled model can provide
127 realistic environmental conditions in the soil layers, troposphere, and ocean surface at high
128 resolution. In this way, a concerted view of thermodynamic conditions from the land and the
129 ocean surface to the upper-level troposphere can be retained throughout the simulation to
130 properly account for the influence of the land surface fluxes on the TC intensity changes after
131 landfall.

132 We implement the NASA Unified-WRF (NU-WRF; Peters-Lidard *et al*., 2015) coupled
133 with NASA's Land Information System (LIS; Kumar *et al*. 2006; Peters-Lidard *et al*. 2007). NU-
134 WRF was developed using the community WRF model (Skamarock *et al*. 2005) to test several
135 physical process parameterizations intended to improve cloud aerosol, precipitation, and land
136 surface processes associated with convective systems on satellite resolvable scales (~1 km
137 horizontal grid resolution). The latest improved version of the Goddard Microphysics scheme

(Goddard 4ICE) can simulate physical processes for cloud ice, snow, graupel, and frozen drops/hail within both intense and moderate convection (Lang *et al*. 2014; Tao *et al*. 2016). These multi-faceted capabilities of the Goddard 4ICE microphysics scheme are considered as critical for the TCMI modeling experiments in this study (refer to supplementary material for details).

At the same time, physical conditions of the land surface (e.g., soil moisture, soil texture, energy balance between the land and atmosphere) can play a critical role in enthalpy supply to landfalling TCs (Andersen *et al*. 2013). To characterize land surface states and fluxes under the landfalling TC accurately, NASA's LIS is coupled with the NU-WRF in our modeling experiments. Noah LSM version 3.6 (Mitchell *et al*. 2005) is employed in LIS to spinup the land surface for five years (i.e., from 00 UTC 1 January 2013 to 00 UTC 16 February 2018) before the coupled NU-WRF simulations of Kelvin are initialized. The LIS spinup is driven by the Global Data Assimilation System (GDAS) data by the National Center for Environmental Prediction (NCEP) Global Forecast System (GFS) model as meteorological forcing. The GFS final analysis (FNL) is used as the model IC/BCs for WRF-LIS coupled simulations (Table 1).

2.3. Experimental Design

In order to answer the key research questions of the TCMI mechanisms of Kelvin, a framework of modeling experiments is established to facilitate intensive numerical model simulations of the target storm. In this study, two suites of physics schemes are used for comparison purposes in the TC experiments: "NU-WRF" and "WRF tropical." They represent the recommended package of physics options for TC or hurricane simulations within the NU-WRF and the WRF model community (WRF Users Guide 2012), respectively.

In the NU-WRF physics suite, cloud microphysics are computed using the Goddard 4ICE (Tao *et al*. 2016), and the longwave/shortwave radiation is calculated using the Goddard 2017 radiation scheme (Matsui *et al*. 2018). Turbulent closure is computed using level 2 of the Mellor-Yamada-Nakanish-Niino (MYNN) model (Nakanishi and Niino 2004, 2006, 2009) in which vertical mixing is parameterized to interact with both planetary boundary layer (PBL) and free atmosphere (Noda *et al*. 2010; Ohno *et al*. 2016). For the WRF tropical suite, on the other hand, cloud microphysics are computed using the WSM6 scheme which solves for six categories of hydrometeor: water vapor, cloud water, cloud ice, rain, snow, and graupel (Hong and Lim 2006). The longwave/shortwave radiation scheme is RRTMG (Iacono *et al*. 2008; Mlawer *et al*. 1997; Iacono *et al*. 2000; Clough *et al*. 2005), and the bulk surface flux is computed using the MM5 Similarity based on Monin-Obukhov similarity functions (Monin and Obukhov 1954). The PBL physics are calculated by Yonsei University PBL scheme (Hong *et al*. 2006).

The following common modeling settings apply to all the simulation cases in this study. The atmospheric model has 61 vertical levels with 50 hPa at the model top. A quasi-uniform horizontal grid spacing of 1 km is used for a 1200 km (latitude) by 1200 km (longitude) single domain over the northwestern Australia (Figure 2). The configured domain size is large enough to understand the land-atmosphere interactions, but may not be sufficient to capture the large-scale (> synoptic scale) TC features as addressed later in this paper. Both model boundary conditions and sea surface temperature are updated every 6 hours. The model integration is computed at the time step of 6 seconds for the four-day simulation from 00 UTC 16 February to 00 UTC 20 February, 2018, producing hourly model output. Table 1 supplies a summary of the NU-WRF/WRF modelling experiments designed for the study. Simulation IDs were assigned to each simulation to facilitate as concise distinctions among the various experiments as possible.

Two sets of preliminary experiments were conducted to select a best-performing combination of a) forcing data from multiple IC/BCs (i.e., the GDAS data, Modern-Era Retrospective Analysis for Research and Applications, version 2 (MERRA-2; Gelaro *et al*. 2017), and the European Center for Medium range Weather Forecasting (ECMWF) ERA-Interim (ERAI; Dee *et al*. 2011; Berrisford *et al*. 2011)) and b) model physics (i.e., NU-WRF vs. WRF tropical) for the Kelvin case among many permutations (see Table S1, Physics and BC Ensemble Experiments Parts I and II in the supplementary material). The IC/BC performance and the impacts of the Goddard versus WRF physics options on TC track and intensity were examined in advance of this study, descriptions of which are provided in the supplementary material.

Then, the best performing model configuration of IC/BCs and physics is used to explore the storm sensitivity to variation components relevant to the BOE such as soil moisture, soil texture, model physics, and surface latent/heat flux to quantify the role of land and atmospheric processes in landfalling TC intensification (Table 1, Land/soil moisture perturbation experiments). Three different soil texture configurations are compared using the NCEP/FAO soil texture in 30 arc-sec resolution (Control) which is the default soil texture setting in the WRF and the LIS models, the ISRIC soil texture at 250 m resolution (ISRIC; see Hengl *et al*. 2015, 2017 for details) and a constant soil texture of clay over land in the 30 arc-sec resolution (Clay) (Figure 2). Variations in soil moisture conditions range from extreme (i.e., no latent heat flux (LHzero), no sensible heat flux (SHFzero), and no latent and sensible heat flux (LSHFzero)), through pseudo-climatological dry and wet (SMdry and SMwet), then fully saturated at soil type maximum (SMsat), to a quasi-aqua planet condition (SMaqua). The "WRF tropical" physics options are also applied to the SMdry and SMwet soil moisture conditions, which are SMdrytropic and SMwettropic, respectively (See Table 2). These permutations of surface

moisture, moisture fluxes, and soil type are designed to isolate and control for the specific impacts of the land surface moisture on TC Kelvin's track and intensity. The specific motivating questions and simulations details for all the experiments conducted are available in the supplementary material.

3. Results

3.1. Influence of Land Surface and Soil Moisture Conditions

Simulated storm tracks from the cases using the NU-WRF physics (NU-WRF cases, hereafter), that made landfall in the low-level plain valley of Kimberley and Pilbara regions in the northwest Australia, show a good consensus (Fig. 3a) despite differences in their intensities, which begin to diverge near intensification on 17 February before landfall (Fig. 3b). The mean track errors of the NU-WRF cases were comparable to that of Control with 43.2 km (see Table 2). In contrast, the errors of the WRF tropical suite cases were larger by a factor of about two. Figure 3b shows that all the other NU-WRF cases produced their intensity trend relatively close to the Control except LSHFzero, SMwettropic, and SMdrytropic. In particular, they all reproduced the main intensification on 17 February as supported by the IBTrACS and SATCON observational records (see Fig. S1 in the supplementary material). In contrast the LSHFzero, the SMwettropic, and SMdrytropic intensified on 17 February but their magnitudes were even less than the Best track record by the Australian BoM (Fig. 3b.) Note also that the landfall times of SMwettropic and SMdrytropic were much earlier than the others.

Regardless of the model physics employed, each simulation reproduced the secondary intensification inland on 19 February except for LHzero and LSHFzero. This analysis suggests that despite rather extreme permutations of the land surface moisture and energy fluxes, the

simulated track and intensity were predominantly regulated by other (atmospheric) factors while the spectrum of the land surface moisture and energy fluxes exerted secondary influence on the simulated storm intensity post-landfall.

3.2. Radar Reflectivity Assessment of TC Kelvin

Understanding the impacts of the modified land surface conditions on the simulated storm can be leveraged by comparing the horizontal distribution of convective activities within the TC environment itself. Figure 4 shows simulated composite radar reflectivity on 19 February at 12 UTC when Kelvin went into the second intensification inland more than 300 km away from the coast. The storms in the cases of the LHzero and the LSHFzero were weakened or disorganized compared to the other NU-WRF physics cases, while the storms in the cases of Control, ISRIC, Clay, SHFzero, SMaqua, SMsat, SMdry, and SMwet still maintained eyewall structures and rainbands at that time. Close comparisons also provide subtle differences in convective activities around the core and the surrounding environment. The storm in the Control run was intensifying (noted with red dot in the eye in Fig. 4) and the storm structure was clearly maintained. The ISRIC and the SMdry show a similar reflectivity pattern as in Control but their intensity was not changing (noted with gray dot in the eye). The storm in the Clay, the SMaqua, the SMsat, and the SMwet case was intensifying but storm structure was slightly degraded compared to the Control. The storm in the SHFzero was weakening (noted with blue dot in the eye) while its intensity was comparable to the Control.

3.3. Diurnal Cycle of Surface Energy Budget

It is well known that the atmospheric radiative forcing processes of differential warming (i.e., in the core region) and cooling (i.e., in the outer region) within the TC environment are closely related to nighttime intensifications of convective activities in TCs over the ocean (see

Tang and Zhang 2016 and references therein; Dunion *et al*. 2019). However, none of the previous BOE studies has related the diurnal cycle of surface fluxes to TCMIs. In this section, we address the relationship between them by showing the diurnal cycles of surface energy budgets and TC intensity changes.

Figure 5 shows the time series of the areal sums of the surface fluxes and radiation (i.e., latent heat (LH), sensible heat (HFX), ground flux (GRDFLX), downward longwave (SLWDN), upward longwave (SLWUP), downward shortwave (SSWDN) and upward shortwave (SSWUP)) within the radii of a) 200 km and b) 600 km from the center of the simulated storm along with the time series of the maximum wind speed. Due to thick clouds in the core region within the 200 km radius, longwave radiation dominated in all the NU-WRF cases, which was fairly compensated by the outgoing longwave radiation (Fig. 5a). When the storm was over the ocean, latent heat flux was the second largest among the surface fluxes within the NU-WRF cases, which changed rapidly as the storm moved onto land on 18 February. The LH flux dropped significantly during the nighttime on 18 February. Even at its peak on 19 February, LH flux barely reached 50% of its average over the ocean during 16-17 February. Incoming solar radiation was consistent and exhibited a diurnal cycle clearly even in the core region within the 200 km radius. Ground flux and outgoing solar radiation were relatively small and not significant to the surface energy budget in the TC case. From these results, since not only the main intensification of Kelvin on 17 February but also the secondary inland intensification on 19 February occurred with the onset of local nighttime, it seems that diurnal cycle of convective activity is highly associated with Kelvin's intensity changes. For the cases where intensification did not occur (e.g., the WRF tropical suite cases for the main intensification or LHzero and

LSHFzero for the secondary inland intensification), reasons for their failures should not be directly attributed to the diurnal cycle.

The analysis at 600 km radius (Fig. 5b) shows similar patterns as in the 200 km radius with the exception of incoming solar radiation increasing significantly with the outer region, as expected. The larger solar radiation in the outer region with more cloud-free area can energize the lower atmosphere during the daytime as long as the atmosphere does not become too dry over the land so as to exert an adverse effect to the secondary circulation of the storm. In fact, previous studies noted that the elevated thermodynamic energy in the outer region increases the convective activity in that region during the daytime, which accompanied by the increase of the radius of the maximum wind (RMW); as it shifts into nighttime, atmospheric radiative cooling in the outer region and the relatively delayed cooling or even warming in the core region may have sped up the convergence under the eyewall area, intensifying the storm (Gray and Jacobson 1977; Craig 1996; Tang and Zhang 2016). Therefore, the surface energy budget and the larger solar radiation in the outer region as shown in Fig. 5b suggest that the diurnal cycle mechanism in TC development can be applied in the TCMI of TC Kelvin. Further detail analysis is warranted to show the relationship between the surface fluxes and the diurnal cycle of radiative cooling as one of the potential mechanisms for TCMIs, which is beyond the scope of the current study.

3.4. Influence of the Large-scale Environment

Although BOE studies may tend to focus on the local land surface properties, an understanding of the large-scale environment where TCs evolve is still critical to properly assess the relative impacts of the local land surface on TCMIs. Associated with the SST distribution (Fig. 1a), Figure 6 shows 30 km grid resolution ECMWF ERA5 reanalysis (Copernicus Climate

297 Change Service (C3S) 2017) of Total Column Water (TCW) superimposed by 500 hPa and 850
298 hPa wind vectors over Australia as well as the Pacific and Indian oceans during Kelvin at 20
299 UTC 17 February and 11 UTC 19 February, respectively, when Kelvin presented
300 intensifications. The location of the ITCZ can be inferred by the equatorial band of high TCW.
301 During the same times, Figure 7 shows mean vertically integrated moisture divergence
302 superimposed by 500 hPa wind vectors. The large-scale view of the TCW along with the
303 moisture divergence and wind vectors suggests that the convergence of water vapor to the north
304 of Australia occurred as a consequence of an equatorial Rossby (ER) wave (Matsuno 1966;
305 Kiladis *et al*. 2009). Indeed, Kelvin's twin counterpart on the other side of the equator in the ER
306 wave was Tropical Storm Samba near the Philippines (Dollery 2018). Figures 6 and 7 support
307 that Kelvin's intensifications on both 17 and 19 February had been taking place under the
308 influences of the ER wave and the ITCZ. Note that a band of enhanced water vapor (i.e., TCW)
309 as well as the moisture convergence extend from Kelvin southward to the southern shore of
310 Australia. The southward movement of the vortex (i.e., Kelvin) occurred along with the low-to-
311 mid-level atmospheric moisture advections in the "convergence" area within the ER wave further
312 south into inland Australia. Kelvin is being steered southward by the northerly flow associated
313 with a subtropical ridge to the east and an approaching trough from the west as manifested as the
314 ER wave in the southern hemisphere. These features with successive waves of moisture from the
315 equatorial region may be key factors in the horizontal transport of water vapor, posed to be
316 relevant in the TCMI of Kelvin. Therefore, it should be noted that the main intensification of
317 Kelvin was favored by warm SST and the vortex growth within the ER wave that spun-off from
318 the ITCZ.

Figure 8 shows time series of the mean vertical wind shear between 850-250 hPa levels averaged over the model domain excluding the circular area within the radius of 300 km from the center of the simulated storm. In all cases, the storm was able to intensify despite being influenced by strong deep-layer shear of 16 m s^{-1} on 16 February, whereas the wind shear decreased down to moderate level of 10 m s^{-1} when the storm intensified. Compared to the NU-WRF cases, higher shear prevailed during 17-18 February in the WRF tropical cases, potentially suppressing the intensification of the storm. Since being associated with large-scale interaction between the storm and environment, the vertical wind shear may not be sensitive to the local scale land surface conditions as shown by the similar wind shear time series among the NU-WRF cases.

3.5. Inner-core Thermal Condition and TC Intensity

TC intensity can be determined by the horizontal pressure differences between the vertical pressure profile in the center of the TC and the average of the vertical pressure distributions of the TC's environment, which are dependent on the vertical temperature profiles. Therefore, the horizontal temperature differences of the vertical profiles between the core of a TC and its environment (herein Delta T or dT) are the key proxy of the TC's intensity (Ohno *et al.* 2016). Moreover, the maximum of the horizontal temperature differences (noted as Max_dT), is highly correlated with TC intensity.

Within the context of the BOE, we are interested in the sensitivities of TC intensity (or the Max_dT) to the change of the surface conditions (i.e., soil moisture, energy fluxes, and surface soil type), and thus, we compare time series of the Max_dT and TC intensity within the experiment cases. To compute the dT between the warm-core and the environment, normally the reference profile for the environment is defined by the time-varying mean vertical temperature

342 profile that is spatially averaged over a 550-650 km annulus (Stern and Zhang 2013). However,
343 weaker storms tend to have their inner-core within shorter radii than major storms. Thus, an
344 annulus with smaller radii can be used (e.g., 300-700 km radii in Munsell *et al*. 2018). Since
345 Kelvin was a weak storm (< Category 2), we used a 300-400 km annulus in this study. The
346 warm-core profile was retrieved following the eye of the simulated storm for each case. Profiles
347 of virtual temperature anomalies (Figure 9) represent the warm-core of each simulation case on
348 17 February at 21 UTC and 19 February at 11 UTC when TC Kelvin was intensifying either over
349 ocean or inland, respectively. The images suggest that the warm-core anomaly was present in all
350 the cases on both dates. It is notable that the spread of the warm-core anomalies among
351 experiment cases was larger on 17 February than on 19 February. These warm-core anomalies,
352 especially in the mid-upper levels, lasted to the end of each simulation on 20 February.
353 Among the NU-WRF physics cases, their virtual temperature anomalies are comparable
354 to each other. But closer examination reveals that some cases have achieved larger anomalies in
355 the lower to midlevel atmosphere than the control simulation by 17 February at 21 UTC (e.g.,
356 ISRIC, Clay, and SMaqua). In contrast, the WRF tropical suite physics cases of SMdrytropic and
357 SMwettropic developed the least (i.e., weakest) warm-core anomalies in the mid-upper
358 troposphere (200 - 600 hPa). These results are consistent with the previous findings in this study
359 as well as previous studies suggesting that pronounced upper-level warm-cores are typically not
360 present in weaker TCs.
361 Similarly, Skew-T analyses employing the same 300-400 km annulus reference
362 environment provide the further details of temperature and humidity profiles simultaneously for
363 the two intensification periods on 17 and 19 February (Figs. 10ab). Note that temperature
364 profiles in the eye in the Control run are quite comparable, while dewpoint temperature (i.e.,

humidity) profiles in the eye show that upper-level air (above 300 hPa level) are much drier over land than over ocean. Also, environmental humidity profiles suggest that the mid-level (near 400 hPa) atmosphere over land on 19 February became drier as compared to over ocean on 17 February. These are characteristic features of TCs transitioning from ocean to inland within the experiments in this study (Figs.10df).

Considering all the other cases together, temperature profiles in the eye did not vary much case by case. Relatively, much large variations occurred with the humidity profiles in the eye in the upper-level atmosphere (above 300 hPa level). Temperature and humidity profiles of the reference environment showed the similar pattern as in the eye. Interestingly, ISRIC, Clay, LHzero, SMdry, and SMwet produced slightly more humid environmental profiles than Control near 400 hPa pressure height characteristically on 19 February (not shown); In contrast, SHFzero, LSHFzero, SMaqua, SMsat simulated substantially dry environmental profiles than Control at mid-upper level (600-250 hPa) on 19 February (e.g., Figs. 10cdef). The WRF tropical suite physics cases of SMdrytropic and SMwettropic also had substantially dry upper-level warm-cores. These results suggest that the atmospheric humidity profile is more sensitive to the experimental treatments than the temperature profile both in the eye and the reference environment.

Figure 11 shows the time series of the Max_dT and the maximum wind speed. The highly correspondent trends between the Max_dT and the maximum wind speed as in the Control support that the magnitude of the temperature difference between the warm-core and the environment (i.e., Max_dT) is closely related to the storm's intensity change regardless of the vertical levels where Max_dT occurs. These results are consistent with a few recent studies on TC inner-core temperature structure (e.g. Ohno *et al*. 2016, Munsell *et al*. 2018, and Wang and

Jiang 2019). Since the warm-core anomaly of a TC is achieved mainly by the latent heat release either in the condensation of the water vapor or in the solidification of raindrops (e.g., ice, graupel, or hail) rather than by diabatic heating (e.g., by sensible heat flux), Figure 11 suggests that the lower Max_dT in the cases of the LHzero, LSHFzero, SMdrytropic, and SMwettropic may be attributable to less moisture or less condensation in the atmosphere. This led to less latent heat release in the core of the storm, in these cases compared to the others, resulting in the weaker intensity of the storm. Therefore, Fig. 11 suggests that without any dramatic changes in the land surface moisture conditions, TC Kelvin's intensity is not highly sensitive to the preexisting land surface moisture conditions such as in SMdry or SMwet. Likewise, Fig. 11 shows that alternative soil texture settings (i.e., ISRIC and Clay) had minimal impacts on Max_dT or TC intensity in Kelvin compared to the Control case. However, the magnitude of the dryness of mid-upper-level atmosphere was not directly correlated to the magnitude of warm-core anomaly changes (e.g., Max_dT) in the vertical profile in this study. Thus, further study is warranted for their relationship.

3.6. Relative Influence of Surface Fluxes vs. Total Precipitable Water

The hypothesis of the BOE is based on the assumption that moisture fluxes from the land play a critical role in the TCMIs. In the previous analyses, the various treatments for land surface moisture conditions did not result in outstanding differences in the inland intensification of the TC Kelvin except in a few extreme cases like LHzero and LSHFzero. Therefore, in this section quantities of total atmospheric moisture and moisture flux from the surface are compared to understand the contribution of the land surface moisture flux to the TCMI of Kelvin. At the same time, enthalpy fluxes (i.e., latent heat flux and sensible heat flux) are examined regarding the TCMI feature of TC Kelvin.

411 Figure 12 shows the time series of the mean of hourly total moisture fluxes (QFX [kg m-
412 $^{-2}$]) and Total Precipitable Water (TPW [kg m^{-2}]) for the entire model domain, land, and sea,
413 separately. To facilitate the comparison between the QFX and the TPW, the units of the
414 instantaneous moisture flux (QFX [kg m^{-2} s^{-1}]) were converted to hourly quantity [kg m^{-2}] as the
415 TPW. Figure 12a suggests that moisture flux over the ocean is significantly larger than that over
416 the land within the model domain during the entire period of the simulation. Moisture flux from
417 the land shows clear diurnal cycles and only at their peaks do the land fluxes become comparable
418 to ocean fluxes. It is notable that only SMaqua and SMsat produced substantially large moisture
419 fluxes over land during their diurnal peaks on 16 and 19 February, while those in LHzero and
420 LSHFzero remain zero as intended. Overall, the moisture fluxes over land do not exceed 0.3 kg
421 m^{-2} (about 200 W m^{-2} in latent heat flux) and remain below 0.1 kg m^{-2} most of the time while
422 those over ocean maintain about 0.3 kg m^{-2} throughout the simulation period. This result
423 suggests that the moisture fluxes over the ocean were higher than over the land in general during
424 the simulation period except for extreme land surface situations (e.g., regional floods).
425 In contrast, the TPW exceeded 40 kg m^{-2} at minimum for all the cases, which is more
426 than 100 times the moisture fluxes over land. In addition, the magnitude of TPW in each
427 simulation is remarkably similar in the temporal evolution during TC Kelvin as if the impacts of
428 the surface permutations are negligible (Fig. 12b). Considering the fact that a significant amount
429 of TPW exists in the lower atmosphere below 700 hPa level (>90 %; not shown), the moisture
430 fluxes over land (< 0.3 kg m^{-2}) may not have played a critical role in the intensification of Kelvin
431 as compared to the existing atmospheric moisture volume.
432 Even larger differences between surface moisture fluxes and the TPWs can be gathered
433 via plots of their radial means. Figure 13a suggests that while the center of the storm was over

434 the ocean (on 16-17 February), the actual amounts of areal mean moisture fluxes occurring from
435 the surface (both land and ocean combined) within the inner radii (e.g., 50, 100, and 200 km) of
436 the storm were about 0.4-0.6 kg m^{-2} (even > 0.8 kg m^{-2} at the peak in Control, ISRIC, Clay, and
437 SMdry). Those from the outer radii (e.g., 300, 400, 500, and 600 km) were about 0.18-0.3 kg m^{-2}
438 in general. After landfall (17 February at 21 UTC), the moisture fluxes within the inner radii
439 suddenly plunged down to below 0.1-0.2 kg m^{-2}, meaning that in the Control run about 87% of
440 the surface moisture fluxes decreased at maximum within the 50 km radius. However, those in
441 the outer radii maintained their previous level. The TC obtained TS intensity (> 18 m s^{-1}) on 16
442 February before landfall and maintained at least within the TS intensity after landfall (Fig. 3b).
443 If the storm went through the TCMI event purely because of the surface moisture fluxes
444 (e.g., latent heat fluxes from soil), those quantities within the inner radii after landfall should be
445 at least comparable to those on 16 February. Instead, a more than 50 percent decrease in the
446 latent heat flux within the inner radii after landfall does not support the BOE hypothesis in this
447 case. In contrast, the mean TPW quantity trend remained consistent between the inner and outer
448 radii over ocean and land with relatively gradual decreases after landfall (Fig. 13b). This
449 suggests that even with the limited amount of moisture fluxes from the land, the inner-core of the
450 storm was supported by the moisture supply in the lower atmosphere, which was efficient
451 enough to maintain its structure and even to briefly intensify after landfall. Over the ocean, the
452 surface moisture flux under the eyewall should be at a maximum due to the maximum wind (Fig.
453 13a). After landfall, however, the surface moisture fluxes within the 50 km radius became less
454 than 1/300 of the TPW in general. It is possible that the contributions of surface moisture fluxes
455 in the outer radii exceeded those in the inner radii due to larger solar radiation resulting from less

456 cloud cover in the outer radii as thick convective clouds around the eyewall reduce radiation in
457 the inner radii.

458 In terms of latent heat flux, the mean of moisture flux over land did not exceed 200 W m^{-2}
459 during the peak of the day and remained below 50 W m^{-2} during the night (Fig. 14a) in most
460 cases. Exceptionally, however, mean LH fluxes in the SMaqua and the SMsat easily exceeded
461 200 W m^{-2} during the days reaching up to about 500 W m^{-2} on 16 February and 350 - 400 W m^{-2}
462 on 19 February. Their nighttime LH fluxes were also slightly increased before landfall, but
463 decreased to below 50 W m^{-2} during the nights after landfall. Treatments of drying and wetting
464 soil (i.e., SMdry and SMwet) as the initial condition resulted in negative and positive LH flux
465 responses during the day over land, respectively, compared to the control simulation. The effects
466 of dry or wet soil moisture conditions at the initial time were maximum in the first day (<50 W
467 m^{-2} in SMdry vs. > 200 W m^{-2} in SMwet compared to Control of which was about 100 W m^{-2}).
468 The two runs converge gradually towards the magnitude of mean LH flux of the Control by 19
469 February, possibly because concurrent precipitation by the storm may have equalized the soil
470 moisture contents over time in the SMdry and the SMwet. Similar trends were observed with the
471 sensible heat flux (SHF [W m^{-2}]) in the SMdry and the SMwet (Fig. 14b), as the first day SHF
472 was larger in the SMdry and smaller in the SMwet compared to the Control, but the differences
473 are lessened over time. SHFs over land in the SMaqua and the SMsat were very small and those
474 in the SHFzero and the LSHFzero were zero as expected. SHFs in SMdrytropic and SMwettropic
475 also responded to the dry/wet treatments but showed a monotonic change over time unlike the
476 SMdry and the SMwet. Therefore, Figs. 12, 13, and 14 support the previous finding that the
477 moisture fluxes over land did not play a critical role in the inland intensification of Kelvin
478 compared to the existing lower atmospheric moisture.

4. Discussion

The term TCMI can be thought of as a generalized term for the BOE, in that TCMIs refer to any TC that manifests its intensification or maintenance of its strength after landfall by any geophysical mechanism. The BOE, in its hypothesis, specifies the role of the enthalpy fluxes from the land as opposed to those from the ocean for the same manifestation of the TCMIs. In particular, previous studies emphasized the roles of the latent heat flux from the wet soils (e.g., > 70 W m^{-2}; Andersen *et al*. 2013) and the sandy soil type (e.g., Emanuel *et al*. 2008) in TCMI events. However, further research was warranted to identify and quantify the exact mechanisms for the BOE. Krikken and Steeneveld (2012) suggested that the inland reintensification of tropical storm Erin (2007) was primarily associated with 1) an upper-level short-wave trough moving eastward, that caused isentropic lifting and positive vorticity advection to Erin over Oklahoma City, OK in the U.S. and 2) a band of warm and moist advection from the Gulf of Mexico to the east flank of TS Erin with rapid speeds up to 20 m s^{-1} (Arndt *et al*. 2009). The influence of vorticity advection from the upper-tropospheric troughs on TC genesis has long been documented (e.g., Riehl 1948). Likewise, there can be additional mechanisms that are already known in the TC literature but not have been found to be associated with the TCMI events.

From Fig. 14a, it is apparent that the climatological threshold of the latent heat fluxes (> 70 W s^{-2}) from previous studies is satisfied during the daytime after landfall in most simulation cases with NU-WRF physics but not during the nighttime when the inland intensification occurred. It is unclear whether this previously defined threshold applies to nighttime as well as daytime and over what spatial extent it is to be used. Regardless, we found that latent heat flux

from the land was not a driving force in the TCMI of Kelvin. Similarly, although sandy soils have been posited as contributing to BOE in Australia in past storms, our experiments do not suggest a dominant influence of sandy soil on the TCMI of this particular TC.

Nevertheless, the question remains whether latent heat flux from wet soil is the driving force of the TCMI mechanism, more generally, and it should be investigated further with case studies that are more sensitive to land surface moisture conditions. The spectrum of the TC intensity shown in the second intensification (Fig. 3b) and the results of radar reflectivity (Fig. 4) as well as virtual temperature anomaly profiles (Fig. 9) or skew-T plots (Fig. 10) suggest that the land surface enthalpy flux plays a small role in the post-landfall TC structure and intensity changes. In the idealized cases of the LHzero and the LSHFzero, the storm barely maintained the intensity of a Tropical Storm (18-32 m s^{-1}) on 19 February, which suggests that with no latent heat flux from the land surface, the storm may not intensify or maintain its strength at all. In contrast, with the latent heat flux from the land surface available, the storm went through a second intensification inland with a spectrum of intensity achieved, regardless of the NU-WRF or WRF tropical suite physics schemes. The second intensification on the 19 February achieved by the SHFzero (Fig. 3b) demonstrates that sensible heat flux plays less of a role in TC intensity than latent heat flux (i.e., LHzero).

Among the soil texture treatment experiments, the ISRIC showed a comparable result to the Control while the Clay case resulted in less intensification on 19 February. This result suggests that the TC simulation is more sensitive to dominant soil types in the domain than to the finer scale resolution of the soil type in this case. Also, the post-landfall storm does not seem to be as sensitive to the initial dry or wet soil condition as expected. The impacts of the previous soil moisture conditions were overwhelmed by the storm's precipitation. Interestingly, the

SMaqua and the SMsat cases suggest that an abundance of soil moisture alone does not guarantee the maximum intensification, either, although the SMaqua and the SMsat generated the most latent heat fluxes during the daytime among the sensitivity simulations (Fig. 14a). Rather, it is the combination of the solar radiation, soil moisture, and the various atmospheric thermodynamic conditions (e.g., midlevel humidity, atmospheric radiative warming and cooling) that need to be satisfied together to intensify the storm. In the case of Kelvin, the evidence presented here supports a marginal to low sensitivity to soil conditions at best in terms of its intensification drivers. It is likely that each landfalling TC lies somewhere on the continuum from no or minimal to extreme or maximum sensitivity to land surface moisture conditions, and should be investigated systematically as was performed here.

5. Conclusion

In this study, a thorough investigation of TC Kelvin was conducted to understand the dominant mechanisms behind its apparent inland maintenance of TC structure and intensity as well as re-intensification after landfall from the perspective of the Brown Ocean effect. Previous studies suggested that the sandy soil in the northern Australia may contribute to more frequent TCMI events in Australia than in the other continents. In this study, it was hypothesized that the enthalpy fluxes from the land surface should be the primary determinant for the TCMI of TC Kelvin. For the study, 12 four-day simulations for the Land/Soil Moisture perturbation study were executed using the NU-WRF model coupled with LIS (with Noah3.6 land surface model). The numerical experiments were designed to isolate the BOE mechanisms by varying the land surface moisture conditions, surface enthalpy flux conditions, and soil texture conditions. The results were analyzed by comprehensively comparing their respective tracks and intensities,

midlevel atmospheric thermodynamic properties, vertical wind shear, TPW, convective structures, and surface moisture fluxes.

The results suggested that the wide ranging and extreme soil moisture, flux, and texture conditions specified did not make a large difference on the track or intensity of the storm. Only the LHzero and the LSHFzero cases in which latent heat flux was disabled from the land surface, simulated substantially weak storms after landfall. Quantitative analyses of the surface moisture flux and the TPW (Fig. 13) revealed that the mean surface moisture flux within the inner radii of the storm (<= 200 km) decreased more than 50 % after landfall. In contrast, the mean TPW did not decrease as suddenly and TPW within the inner radii remained higher than the outer radii regardless of the landfall. Moreover, the absolute quantity of moisture contributed to the core of the storm (radii $\leq$ 600 km) by the surface moisture fluxes after landfall was substantially small compared to the TPW. In fact, the surface moisture fluxes within the 50 km radius were less than 1/300 of the TPW in general after landfall. Therefore, our research hypothesis was rejected and it was concluded that the TCMI of the TC Kelvin was possible mainly by the support of the atmospheric moisture advection that originated from the ITCZ and gushed into northern Australia associated with an equatorial Rossby (ER) wave. With the support of the moisture advection, it is speculated that the secondary intensification over the land on 19 February was associated with the diurnal cycle of TC deep convection, driven by the differential cooling during the nighttime. Various observation-based products support these findings.

While not a clear-cut BOE case, this study is meaningful in understanding the land vs. atmospheric mechanisms of TC intensification, developing a framework for numerical model experiments to unravel the drivers of the BOE and TCMI for future case studies. This modeling

570 framework as well as the analysis methods will contribute to the advancement of the BOE
571 research that will follow.

572 As with any study involving complex atmospheric phenomenon such as landfalling
573 tropical systems, there are limitations with this study. Foremost, surface observations of soil
574 moisture, fluxes, PBL, etc. in the vicinity of the storm's passage were scarce, in part, due to the
575 remote wilderness of northwestern Australia. Land-atmosphere interactions in the larger-scale
576 were not investigated in this study (e.g., equatorial atmospheric waves and MJO) due to the
577 limited domain size of 1200 km by 1200 km. A larger domain configuration or multiple nested
578 domain setting may improve the model experiment in that regard. Future studies should be able
579 to consider a broad spectrum of the scales of the TCs from local to planetary scale, in particular,
580 since TCs interact with various physical processes across these scales. TC core dynamics related
581 with the surface fluxes (e.g., Kuo *et al*. 2019) and diurnal cycles of radiative cooling of TC
582 atmosphere were not covered in this study, which is beyond the scope of the study at present.
583 Future work and case studies focused on quantifying the BOE are being planned, and will
584 employ land (satellite-based soil moisture) data assimilation (DA) in NASA's LIS, to determine
585 the effect of including more realistic ICs, particularly for strong BOE storms.

Acknowledgments. The authors are grateful to three anonymous reviewers for providing valuable and constructive comments on this work. This research was supported by the NASA Modeling, Analysis, and Prediction (MAP) program (16-MAP16-013). We thank also the NASA LIS core team and Carlos A. Cruz for their support with the NASA LIS and the NU-WRF model, respectively.

References

Andersen, T. K. and J. M. Shepherd, 2014: A global spatiotemporal analysis of inland tropical cyclone maintenance or intensification. *Int. J. Climatol.*, **34**, 391-402, DOI:10.1002/joc.3693.

———, D. E. Radcliffe, and J. M. Shepherd, 2013: Quantifying surface energy fluxes in the vicinity of inland-tracking tropical cyclones. *J. Appl. Meteor. Climatol.*, **52**, 2797–2808, https://doi.org/10.1175/JAMC-D-13-035.1.

Arndt, D. S., J. B. Basara, R. A. McPherson, B. G. Illston, G. D. McManus, and D. B. Demko, 2009: Observations of the overland reintensification of Tropical Storm Erin (2007). *Bull. Amer. Meteor. Soc.*, **90**, 1079-1093.

Berrisford, P., D. P. Dee, P. Poli, R. Brugge, M. Fielding, M. Fuentes, P. W. Kållberg, S. Kobayashi, S. Uppala, A. Simmons, 2011: The ERA-Interim archive version 2.0., ERA Report Series, ECMWF, Shinfield Park, Reading, https://www.ecmwf.int/node/8174.

Braun, S. A., 2010: Reevaluating the role of the Saharan Air Layer in Atlantic tropical cyclogenesis and evolution. *Mon. Wea. Rev.*, **138**, 2007–2037.

———, J. A. Sippel, and D. S. Nolan, 2012: The impact of dry midlevel air on hurricane intensity in idealized simulations with no mean flow. *J. Atmos. Sci.*, **69**, 236–257, doi:10.1175/JAS- D-10-05007.1, 2012.

Clough, S. A., M. W. Shephard, E. J. Mlawer, J.S. Delamere, M. J. Iacono, K. Cady-Pereira, S. Boukabara, and P. D. Brown, 2005: Atmospheric radiative transfer modeling: A summary of the AER codes. *J. Quant. Spectrosc. Radiat. Transfer*, **91**, 233–244.

Copernicus Climate Change Service (C3S), 2017: ERA5: Fifth generation of ECMWF atmospheric reanalyses of the global climate. Copernicus Climate Change Service Climate Data Store (CDS), *accessed on 11 December, 2019,* https://cds.climate.copernicus.eu/cdsapp#!/home.

Craig, G., 1996: Numerical experiments on radiation and tropical cyclones. *Quart. J. Roy. Meteor. Soc.*, **122**, 415–422, doi:10.1002/ qj.49712253006.

Dee, D. P., and Coauthors, 2011: The ERA-Interim reanalysis: configuration and performance of the data assimilation system. *Q. J. R. Meteorol. Soc.*, **137** (656), 553–597.

Dollery, R. 2018: Rossby wave: The little-known phenomenon fueling Tropical Cyclone Kelvin off WA. ABC NEWS. https://www.abc.net.au/news/2018-02-16/rossby-wave-phenomenon-fuels-tropical-cyclone-kelvin/9451796 (Accessed August 15, 2019).

Dunion, J. P., and C. S. Velden, 2004: The impact of the Saharan air layer on Atlantic tropical cyclone activity. *Bull. Amer. Meteor. Soc.*, **85**, 353–365.

———, C. D. Thorncroft, and D. S. Nolan, 2019: Tropical cyclone diurnal cycle signals in a hurricane nature run. *Mon. Wea. Rev.*, **147**, 363-387.

Emanuel, K. E., 2000: A Statistical Analysis of Tropical Cyclone Intensity. *Mon. Wea. Rev.*, **128**, 1139-1152.

———, J. Callaghan and P. Otto, 2008: A Hypothesis for the Redevelopment of Warm-Core Cyclones over Northern Australia. *Mon. Wea. Rev.*, **136**, 3863-3872.

Gelaro, R., and Coauthors, 2017: The Modern-Era Retrospective Analysis for Research and Applications, Version 2 (MERRA-2). *J. Climate*, **30**, 5419–5454, https://doi.org/10.1175/JCLI-D-16-0758.1.

Gray, W. M., 1968: Global view of the origin of tropical disturbances and storms. *Mon. Wea. Rev.*, **96**, 669–700.

———, 1998: The formation of tropical cyclones. *Meteorol. Atmos. Phys.* **67**, 37-69.

———, and R. W. Jacobson Jr., 1977: Diurnal variation of deep cumulus convection. *Mon. Wea. Rev.*, **105**, 1171–1188, doi:https://doi.org/10.1175/1520-0493(1977)105<1171:DVODCC>2.0.CO;2.

Hengl T., G. B. M. Heuvelink, B. Kempen, J. G. B. Leenaars, M. G. Walsh, K. D. Shepherd, *et al*., 2015: Mapping Soil Properties of Africa at 250 m Resolution: Random Forests Significantly Improve Current Predictions. *PLoS ONE,* 10(6): e0125814. doi:10.1371/journal.pone.0125814

———, J. Mendes de Jesus, G. B. M. Heuvelink, M. Ruiperez, M. Kilibarda, A. Blagotic, *et al*., 2017: SoilGrids250m: Global gridded soil information based on machine learning. *PLoS ONE,* 12(2): e0169748. doi:10.1371/journal.pone.0169748.

Hong, S. and J. Lim, 2006: The WRF Single-Moment 6-Class Microphysics Scheme (WSM6). *J. Korean Meteo. Soc.*, **42**, 129-151.

———, Y. Noh, and J. Dudhia, 2006: A new vertical diffusion package with an explicit treatment of entrainment processes. *Mon. Wea. Rev.*, **134**, 2318-2341.

Iacono, M. J., E. J. Mlawer, S. A. Clough, and J.-J. Morcrette, 2000: Impact of an improved longwave radiation model, rrtm, on the energy budget and thermodynamic properties of the ncar community climate model, ccm3. *J. Geophys. Res.*, **105**:14873–14890.

———, J. S. Delamere, E. J. Mlawer, M. W. Shephard, S. A. Clough, and W. D. Collins, 2008: Radiative forcing by long-lived greenhouse gases: Calculations with the AER radiative transfer models. *J. Geophys. Res.*, **113**.

Kaplan, J. and M. DeMaria, 1995: A simple empirical model for predicting the decay of tropical cyclone winds after landfall. *Journal of Applied Meteorology*, **34(11)**, 2499-2512.

Kiladis, G. N., M. C. Wheeler, P. T. Haertel, and P. E. Roundy, 2009: Convectively coupled equatorial waves. *Rev. Geophys.*, **47**, RG2003.

Kinghorn, J., 2018: 3 New names and the Brown Ocean Effect. AIR A Verisk Business. https://www.air-worldwide.com/Blog/3-New-Names-and-the-Brown-Ocean-Effect/ (Accessed August 12, 2019).

Krikken, F. and G.-T. Steeneveld, 2012: Modelling the re-intensification of tropical storm Erin (2007) over Oklahoma: understanding the key role of downdraft formulation. *Tellus A*, **64**, 17417, http://dx.doi.org/10.3402/tellusa.v64i0.17417.

Kumar, S. V., C. D. Peters-Lidard, Y. Tian, P. R. Houser, J. Geiger, S. Olden, L. Lighty, J. L. Eastman, B. Doty, P. Dirmeyer, J. Adams, K. Mitchell, E. F. Wood and J. Sheffield, 2006: Land Information System - An Interoperable Framework for High Resolution Land Surface Modeling. *Environ. Modell. Softw.*, **21**, 1402-1415.

Kuo, H.-C., S. Tsujino, C.-C. Huang, C.-C. Wang, K. Tsuboki, 2019: Diagnosis of the dynamic efficiency of latent heat release and the rapid intensification of Supertyphoon Haiyan (2013). *Mon. Wea. Rev.*, **147**, 1127-1147.

Lang, S., W.-K. Tao, J.-D. Chern, D. Wu, and X. Li, 2014: Benefits of a 4th ice class in the simulated radar reflectivities of convective systems using a bulk microphysics scheme, *J. Atmos. Sci.*, **71**, 3583-3612.

Matsui, T., S.Q. Zhang, S.E. Lang, W.- K. Tao, C. Ichoku, C. D. Peters- Lidard, 2018: Impact of radiation frequency, precipitation radiative forcing, and radiation column aggregation on convection-permitting West African monsoon simulations. *Clim. Dyn.* https://doi.org/10.1007/s00382-018-4187-2.

Matsuno, T., 1966: Quasi-geostrophic motions in the equatorial area. *J. Meteor. Soc. Japan*, **44**, 25-43.

Mitchell, K., *et al*., 2005: The Community Noah Land-Surface Model (LSM) User's Guide Public Release Version 2.7.1., NCEP, NOAA.

Mlawer, E.J., S.J. Taubman, P.D. Brown, M. J. Iacono, and S. A. Clough, 1997: Radiative transfer for inhomogenerous atmospheres: Rrtm, a validated correlated-k model for the longwave. *J. Geophys. Res.*, **102**(16663-16682),.

Monin, A.S. and A.M. Obukhov, 1954: Basic Laws of Turbulent Mixing in the Surface Layer of the Atmosphere. *Contrib. Geophys. Inst. Acad. Sci.* USSR, **24**, 163-187.

Munsell, E. B., F. Zhang, S. A. Braun, J. A. Sippel, and A. C. Didlake, 2018: The inner-core temperature structure of Hurricane Edouard (2014): Observations and ensemble variability. *Mon. Wea. Rev*., 146, 135–155, https://doi.org/10.1175/ MWR-D-17-0095.1.

Nakanishi, M., and H. Niino, 2004: An improved Mellor–Yamada level-3 model with condensation physics: Its design and verification. *Bound.-Layer Meteor.*, **112**, 1–31, doi:https://doi.org/10.1023/B:BOUN.0000020164.04146.98.

———, and ———, 2006: An improved Mellor–Yamada level-3 model: Its numerical stability and application to a regional prediction of advection fog. *Bound.-Layer Meteor.*, **119**, 397–407, doi:https://doi.org/10.1007/s10546-005-9030-8.

———, and ———, 2009: Development of an improved turbulence closure model for the atmospheric boundary layer. *J. Meteor. Soc. Japan*, **87**, 895–912, doi:https://doi.org/10.2151/jmsj.87.895.

Niyogi, D., S. Subramanian, and K. K. Osuri, 2016: The role of land surface processes on tropical cyclones: Introduction to land surface models. U. C. Mohandty and S. G. Gopalakrishnan, Advanced Numerical Modeling and Data Assimilation Techniques for Tropical Cyclone Prediction, DOI 10.5822/978-94-024-0896-6_8, Capital Publishing Company.

Noda, A. T., K. Oouchi, M. Satoh, H. Tomita, S.-i. Iga, and Y. Tsushima, 2010: Importance of the subgrid-scale turbulent moist process: Cloud distribution in global cloud-resolving simulations. *Atmos. Res.*, **96**, 208–217, doi:https://doi.org/10.1016/j.atmosres.2009.05.007.

Ohno, T., M. Satoh, and Y. Yamada, 2016: Warm cores, eyewall slopes, and intensities of tropical cyclones simulated by a 7-km-mesh global nonhydrostatic model. *J. Atmos. Sci.*, **73**, 4289–4309, https://doi.org/10.1175/JAS-D-15-0318.1.

Peters-Lidard, C. D., P. R. Houser, Y. Tian, S. V. Kumar, J. Geiger, S. Olden, L. Lighty, B. Doty, P. Dirmeyer, J. Adams, K. Mitchell, E. F. Wood and J. Sheffield, 2007: High-performance Earth system modeling with NASA/GSFC's Land Information System. *Innovations Syst. and Softw. Eng*., 3(3), 157-165.

———, E. M. Kemp, T. Matsui, J. A. Santanello, Jr., S. V., Kumar, J. P. Jacob, T. Clune, W.-K. Tao, M. Chin, A. Hou, J. L. Case,, D. Kim, K.-M. Kim, W. Lau, Y. Liu, J.-J. Shi, D. Starr, Q. Tan, Z. Tao, B. F. Zaitchik, B. Zavodsky, S. Q. Zhang, M. Zupanski, 2015: Integrated modeling of aerosol, cloud, precipitation and land processes at

satellite-resolved scales, *Environ. Modell. Softw.*, **67**, 149–159. doi:http://dx.doi.org/10.1016/j.envsoft.2015.01.007

Riehl, H., 1948: On the formation of typhoons. *J. Meteor.*, **5**, 247–265, doi:https://doi.org/10.1175/1520-0469(1948)005<0247:OTFOT>2.0.CO;2.

Santanello, J. A., Jr., and Coauthors, 2018: Land–atmosphere interactions: The LoCo Perspective. *Bull. Amer. Meteor. Soc.*, **99**, 1253–1272, https://doi.org/10.1175/BAMS-D-17-0001.1.

Skamarock, W. C., J. B. Klemp, L. Dudhia, D. O. Gill, D. M. Barker, W. Wang, and J. G. Powers, 2005: A description of the advanced research WRF Version 2, NCAR Tech. Note TN-4681STR, 88 pp., Natl. Cent. for Atmos. Res., Boulder, Colo.

Stern, D. P., and F. Zhang, 2013: How does the eye warm? Part I: A potential temperature budget analysis of an idealized tropical cyclone. *J. Atmos. Sci*., **70**, 73–90, doi:10.1175/ JAS-D-11-0329.1.

Tang, X., and F. Zhang, 2016: Impacts of the diurnal radiation cycle on the formation, intensity, and structure of Hurricane Edouard (2014). *J. Atmos. Sci.*, **73**, 2871–2892, https://doi.org/10.1175/JAS-D-15-0283.1.

Tao, W.-K., D. Wu, S. Lang, J.-D. Chern, C. Peters-Lidard, A. Fridlind, and T. Matsui, 2016: High-resolution NU-WRF simulations of a deep convective-precipitation system during MC3E: Further improvements and comparisons between Goddard microphysics schemes and observations. *J. Geophys. Res.: Atmospheres,* **121,** 1278-1305. https://doi.org/10.1002/2015JD023986.

Wang, X., and H. Jiang, 2019: A 13-year global climatology of tropical-cyclone warm-core structures from AIRS data. *Mon. Wea. Rev*., **147**(3), 773-790. https://doi.org/10.1175/MWR-D-18-0276.1.

Yoo, J., J. Galewsky, S. J. Camargo, R. Korty, R. Zamora, 2016: Dynamical downscaling of tropical cyclones from CCSM4 simulations of the Last Glacial Maximum. *J. Adv. Model. Earth Syst.,* **8**, 1229-1247, doi:10.1002/2016MS000685.

LIST OF FIGURES

stars (squares) along with their annotations for the times. Red, blue, or gray filled circle both on the Best track and the simulated storm's track represents the storm's tendency of intensifying, decreasing, or maintaining strength compared to the previous time step. The current intensities of the storm at the location are alluded to the size of the circle among the panels. Landfall locations are marked with "⊗" along with their time annotation.

Figure 5. Time series of the areal sum of the surface fluxes (i.e., latent heat (LH), sensible heat (HFX), ground flux (GRDFLX), downward longwave (SLWDN), upward longwave (SLWUP), downward shortwave (SSWDN) and upward shortwave (SSWUP)) within the radii of a) 200 km and b) 600 km from the center of the simulated storm. Black dotted line represents the time series of the maximum wind speed of the storm for each case.

Figure 6. 30 km grid resolution ECMWF ERA5 reanalysis of Total Column Water (TCW) superimposed by 500 hPa and 850 hPa wind vectors over Australia as well as the Pacific and Indian oceans during the TC Kelvin at 20 UTC 17 February (top) and at 11 UTC 19 February (bottom), respectively.

Figure 7. As in Figure 6 but for mean vertically integrated moisture divergence superimposed by 500 hPa wind vectors.

Figure 8. Time series of the areal means of the 850-250 hPa vertical wind shear averaged beyond the radius of 300 km from the center of the simulated storm.

Figure 9. Profiles of virtual temperature anomalies between the eye and the reference environment over a 300-400 km annulus on 17 February at 21 UTC (top) and 19 February at 11 UTC (bottom).

Figure 10. Skew T Log P plots of Control (a and b), SMaqua (c and d), and SMsat (e and f) on 17 February at 21 UTC when the TC Kelvin was intensifying vigorously over ocean (left column) and on 19 February at 12 UTC when the storm was intensifying inland (right column). For Control case, temperature profile at the eye is represented by red line, while temperature profile of the reference environment annular is represented by blue line. Also, dewpoint temperature profile at the eye is represented by red dashed line, while dewpoint temperature profile of the reference environment annular is represented by blue dashed line. For the other cases, likewise, purple and orange colors are used to represent for the eye and the reference environment annular, respectively, along with those for the Control.

Figure 11. Time series of the maximum of the horizontal temperature differences of the vertical profiles between the warm-core and its environment and the maximum wind speed. Those of the Control case (the red line for wind speed and the dotted orange line for Max_dT) are also shown in the other panels for the direct comparisons to those of each case (the green line for wind speed and the dotted blue line for Max_dT).

Figure 12. a) Time series of the mean of hourly total moisture fluxes (QFX [kg m^{-2}]) for the entire model domain, land, and sea; b) Time series of Total Precipitable Water (TPW [kg m^{-2}]) that are areal averages of the model entire domain, land, and sea.

Figure 13. a) Time series of the means of hourly total moisture fluxes (QFX) [kg m^{-2}] averaged within the radii of 50, 100, 200, 300, 400, 500, and 600 km from the center of the simulated storm; b) as in a) but for Total Precipitable Water (TPW [kg m^{-2}]).

Figure 14. Time series of the mean of a) latent heat fluxes (LH [W m^{-2}]) and b) sensible heat fluxes (SHF [W m^{-2}]) for the entire model domain, land, and sea.

LIST OF TABLES

Tables

Table 1. NU-WRF model experiment configurations for the land/soil moisture perturbation experiments

Land/soil moisture perturbation experiments. *Storm sensitivity to land surface fluxes by soil moisture, soil texture, surface flux settings*										
#	Simulation ID	Soil Moisture Sensitivity Simulation Composition Name	IC/BC	Spinup (Forcing)	Physics	mp	radiation	pbl	sfclay	surface
1	Control	NUWRF(GDAS)-LIS(GDAS)	GDAS	LIS(GDAS)	NUWRF	Goddard 4ICE	Goddard 2017	MYNN2	MYNN2	Noah3.6
2	SMwet	NUWRF(GDAS)-LIS(GDAS)-WET	GDAS	Max_Climatology	NUWRF	Goddard 4ICE	Goddard 2017	MYNN2	MYNN2	Noah3.6
3	SMdry	NUWRF(GDAS)-LIS(GDAS)-DRY	GDAS	Min_Climatology	NUWRF	Goddard 4ICE	Goddard 2017	MYNN2	MYNN2	Noah3.6
4	SMsat	NUWRF(GDAS)-LIS(GDAS)-Saturated	GDAS	LIS(GDAS)	NUWRF	Goddard 4ICE	Goddard 2017	MYNN2	MYNN2	Noah3.6
5	SMaqua	NUWRF(GDAS)-LIS(GDAS)-aqua	GDAS	LIS(GDAS)	NUWRF	Goddard 4ICE	Goddard 2017	MYNN2	MYNN2	Noah3.6
6	LHzero	NUWRF(GDAS)-LIS(GDAS)-NoLHF	GDAS	LIS(GDAS)	NUWRF	Goddard 4ICE	Goddard 2017	MYNN2	MYNN2	Noah3.6
7	SHFzero	NUWRF(GDAS)-LIS(GDAS)-NoSHF	GDAS	LIS(GDAS)	NUWRF	Goddard 4ICE	Goddard 2017	MYNN2	MYNN2	Noah3.6
8	LSHFzero	NUWRF(GDAS)-LIS(GDAS)-NoLHF-NoSHF	GDAS	LIS(GDAS)	NUWRF	Goddard 4ICE	Goddard 2017	MYNN2	MYNN2	Noah3.6
9	Clay	NUWRF(GDAS)-LIS(GDAS)-All_Clay	GDAS	LIS(GDAS)	NUWRF	Goddard 4ICE	Goddard 2017	MYNN2	MYNN2	Noah3.6
10	ISRIC	NUWRF(GDAS)-LIS(GDAS)-ISRIC_Soil_Texture	GDAS	LIS(GDAS)	NUWRF	Goddard 4ICE	Goddard 2017	MYNN2	MYNN2	Noah3.6
11	SMwettropic	WRF(GDAS)-LIS(GDAS)-WET	GDAS	Max_Climatology	WRF-Tropical	WSM6	RRTMG	YSU	MM5 Simil.	Noah3.6
12	SMdrytropic	WRF(GDAS)-LIS(GDAS)-DRY	GDAS	Min_Climatology	WRF-Tropical	WSM6	RRTMG	YSU	MM5 Simil.	Noah3.6

Table 2. Experimental land/soil moisture perturbation settings and mean track error results

#	Simulation ID	Soil Moisture Condition	Surface Flux Control	Soil Texture Condition	Mean Track Error (km)
1	Control	Default as forced by GDAS	default	NCEP/FAO	43.2
2	SMwet	Initialized with pseudo-climatologically driest value	Default	NCEP/FAO	44.9
3	SMdry	Initialized with pseudo-climatologically driest value	Default	NCEP/FAO	40.6
4	SMsat	Set as saturated at soil type's maximum	Default	NCEP/FAO	59
5	SMaqua	Set as 1 for quasi-aqua planet condition	Default	NCEP/FAO	59
6	LHzero	Default as forced by GDAS	no latent heat flux transferred to atmosphere	NCEP/FAO	49.3
7	SHFzero	Default as forced by GDAS	no sensible heat flux transferred to atmosphere	NCEP/FAO	52.6
8	LSHFzero	Default as forced by GDAS	no latent/sensible heat flux transferred to atmosphere	NCEP/FAO	56.6
9	Clay	Default as forced by GDAS	Default	a constant soil texture of clay implemented over land	42.5
10	ISRIC	Default as forced by GDAS	Default	ISRIC_Soil_Texture implemented	41.5
11	SMwettropic	Initialized with pseudo-climatologically wettest value	Default	NCEP/FAO	88.3
12	SMdrytropic	Initialized with pseudo-climatologically driest value	Default	NCEP/FAO	82.9

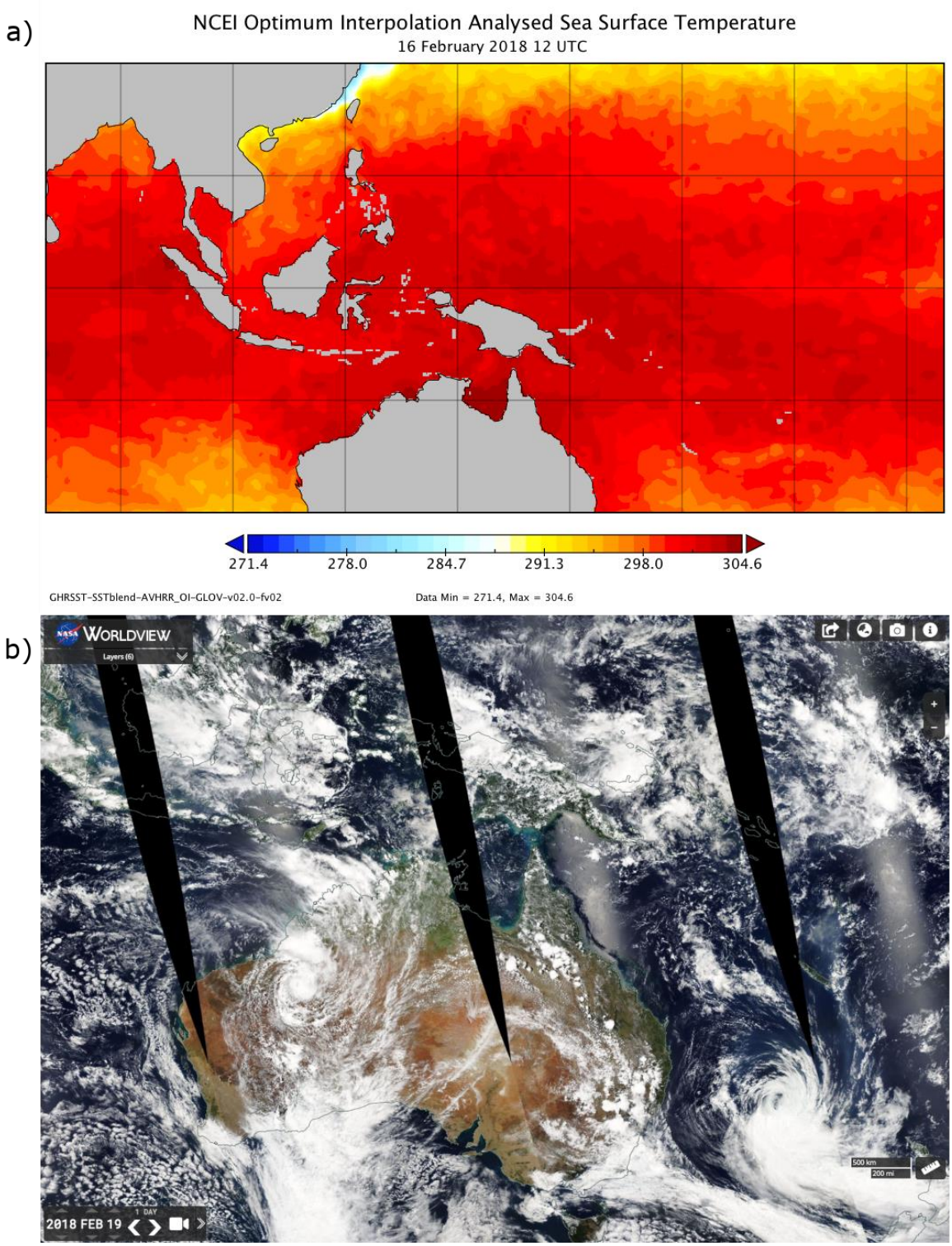

Figure 1 a) NCEI optimum interpolation (OI) sea surface temperature (SST) on 16 February 2018 at 12 UTC; b) Corrected reflectance true color image of MODIS onboard of Aqua satellite overpassing the TC Kelvin inland Australia on February 19, 2018 between 0520-0525 UTC. (Image obtained from the NASA Worldview; https://worldview.earthdata.nasa.gov/).

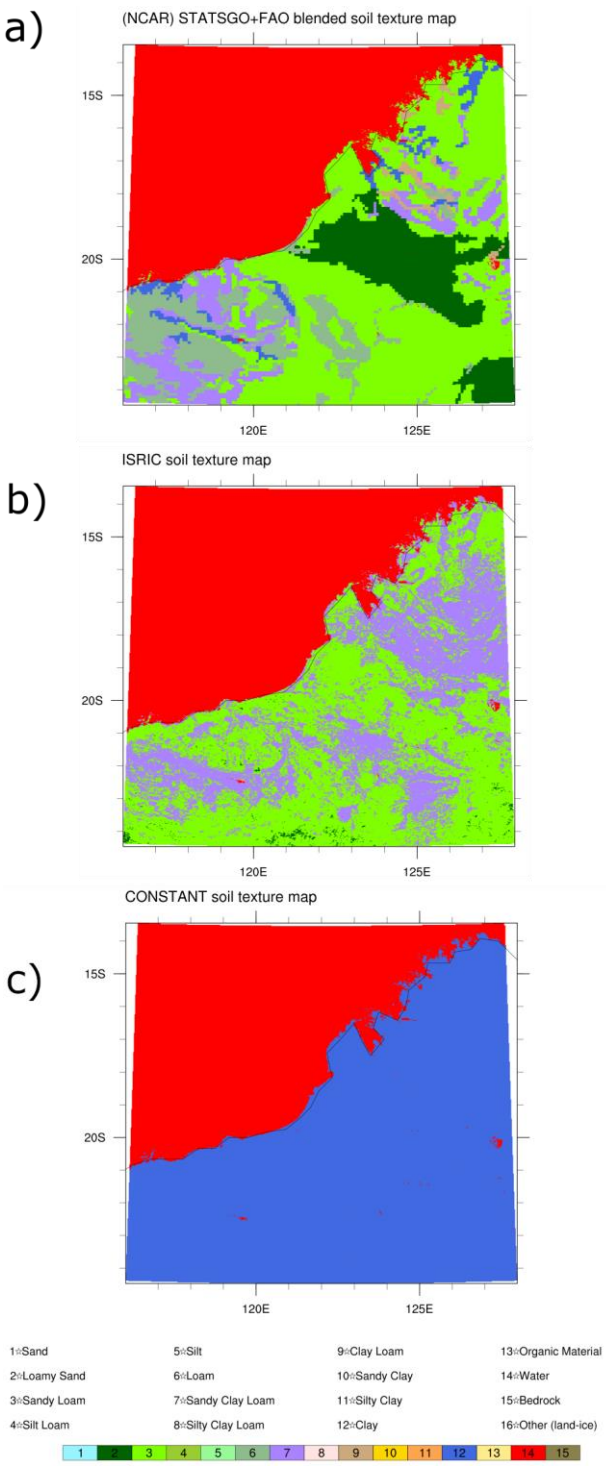

Figure 2. Soil texture options that are employed in this study: a) STATSGO+FAO, b) ISRIC, and c) Constant soil texture of clay exclusively over land.

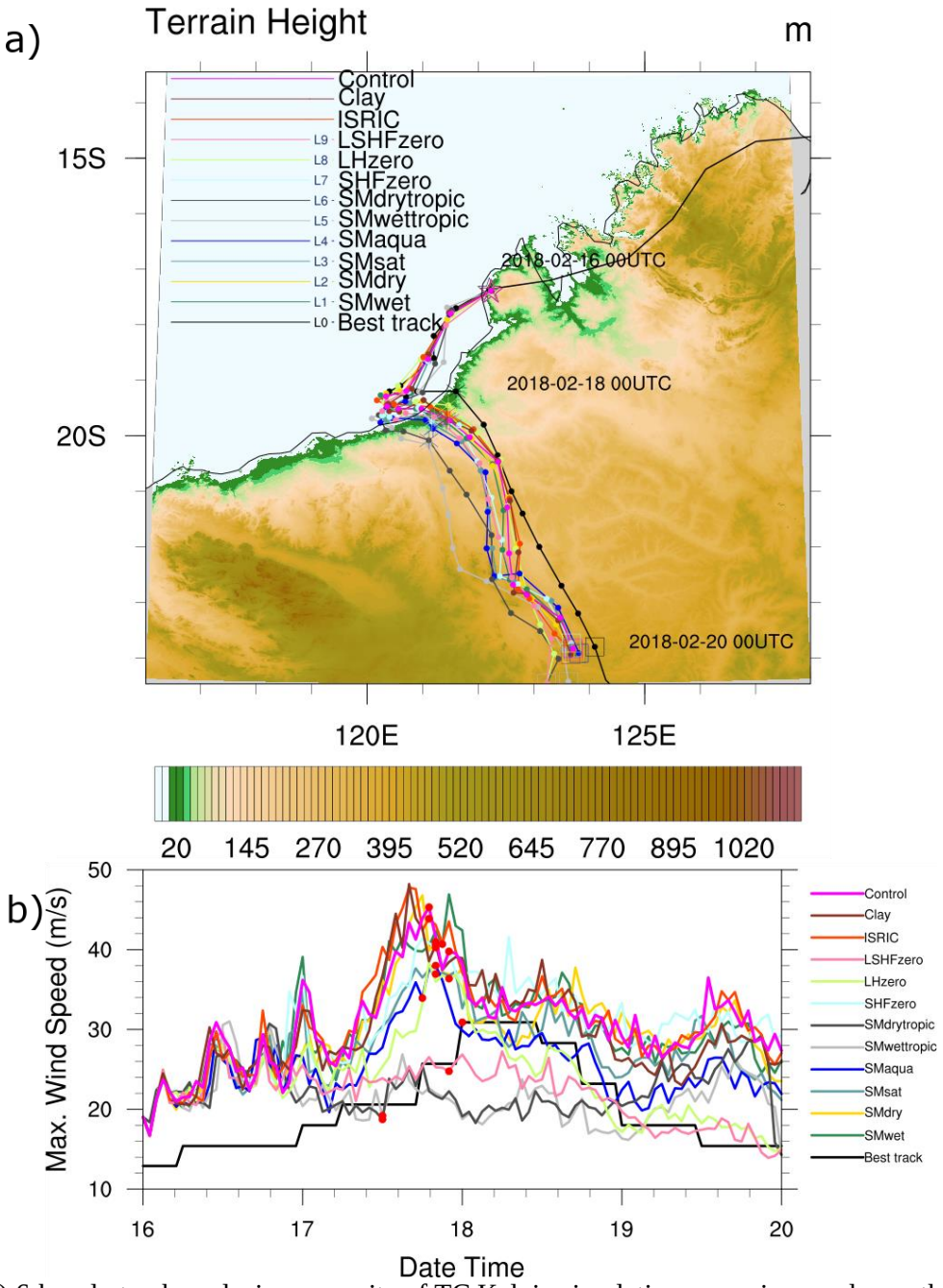

Figure 3. a) 6-hourly track analysis composite of TC Kelvin simulations superimposed over the model terrain height in the Land/Soil Moisture perturbation study and b) time series of hourly maximum wind speed. Labels in legend are consistent with simulation IDs in Table 1. Black line represents the observed track of Kelvin by the Australian Bureau of Meteorology (here, labelled as "Best track"). Storm's 6-hourly center locations of the Best track were plotted with filled circles only for the simulation period (February 16-20, 2018). The initial (final) locations of the simulated storm centers are marked with stars (squares) along with their annotations for the times. Red dots in b) represent the time when the storm moved from ocean to land (i.e., landfall). See Figure 11 for one-to-one wind speed comparisons between the Control and each case.

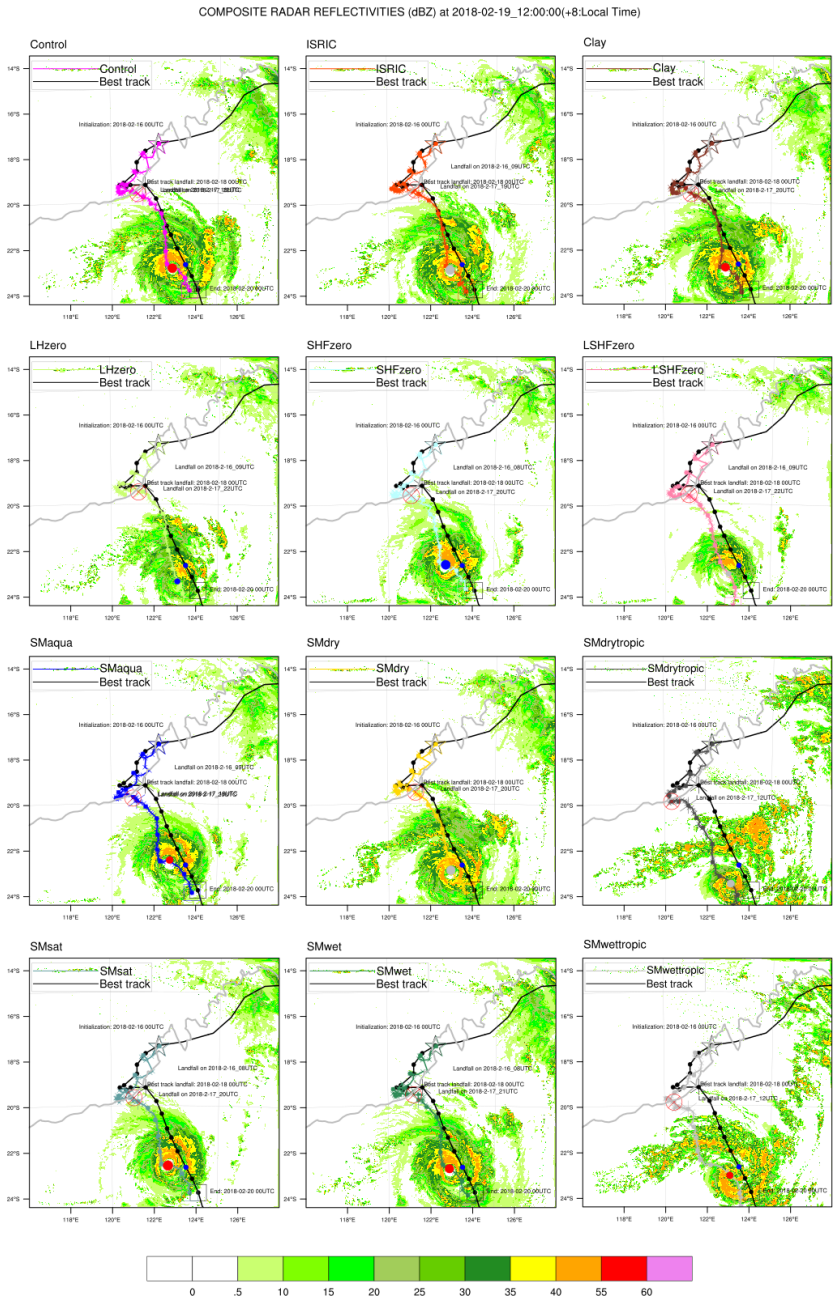

Figure 4. Simulated composite radar reflectivity on 19 February at 12 UTC. Black line represents the observed track of Kelvin by the Australian Bureau of Meteorology (here, labelled as "Best track"). Both Best track and simulated storm's 6-hourly center locations were plotted with filled circles for the entire simulation period (16-20 February, 2018). Note that the storm's current position was not interpolated from the 6-hourly Best track so that the Best track position changes only 6-hourly while the simulated storm's locations move hourly. The initial (final) locations of the simulated storm centers are marked with stars (squares) along with their annotations for the times. Red, blue, or gray filled circle both on the best track and the simulated storm's track represents the storm's tendency of intensifying, decreasing, or maintaining strength compared to the previous time step. The current intensities of the storm at the location are alluded to the size of the circle among the panels. Landfall locations are marked with "⊗" along with their time annotation.

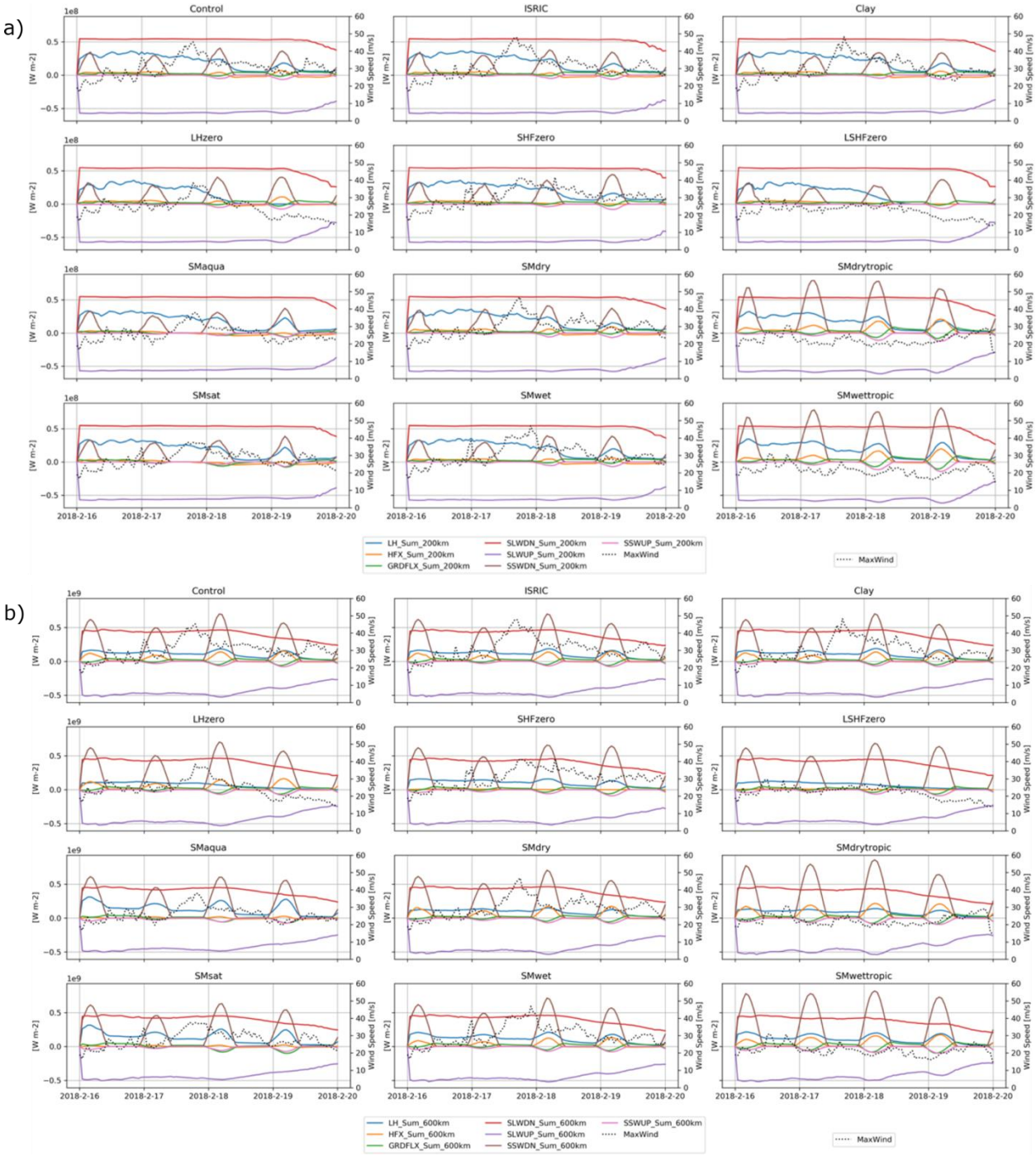

Figure 5. Time series of the areal sum of the surface fluxes (i.e., latent heat (LH), sensible heat (HFX), ground flux (GRDFLX), downward longwave (SLWDN), upward longwave (SLWUP), downward shortwave (SSWDN) and upward shortwave (SSWUP)) within the radii of a) 200 km and b) 600 km from the center of the simulated storm. Black dotted line represents the time series of the maximum wind speed of the storm for each case.

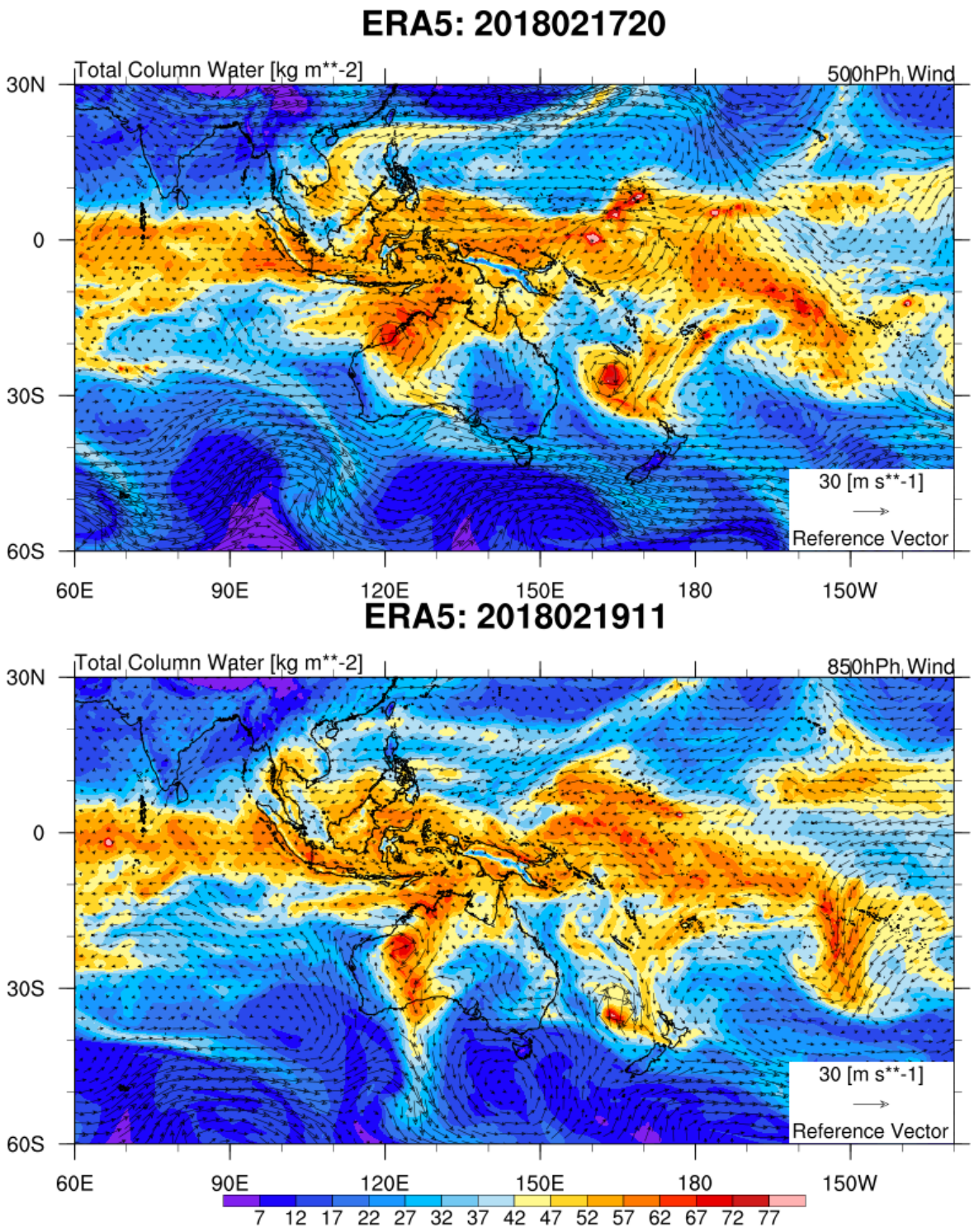

Figure 6. 30 km grid resolution ECMWF ERA5 reanalysis of Total Column Water (TCW) superimposed by 500 hPa and 850 hPa wind vectors over Australia as well as the Pacific and Indian oceans during the TC Kelvin at 20 UTC 17 February (top) and at 11 UTC 19 February (bottom), respectively.

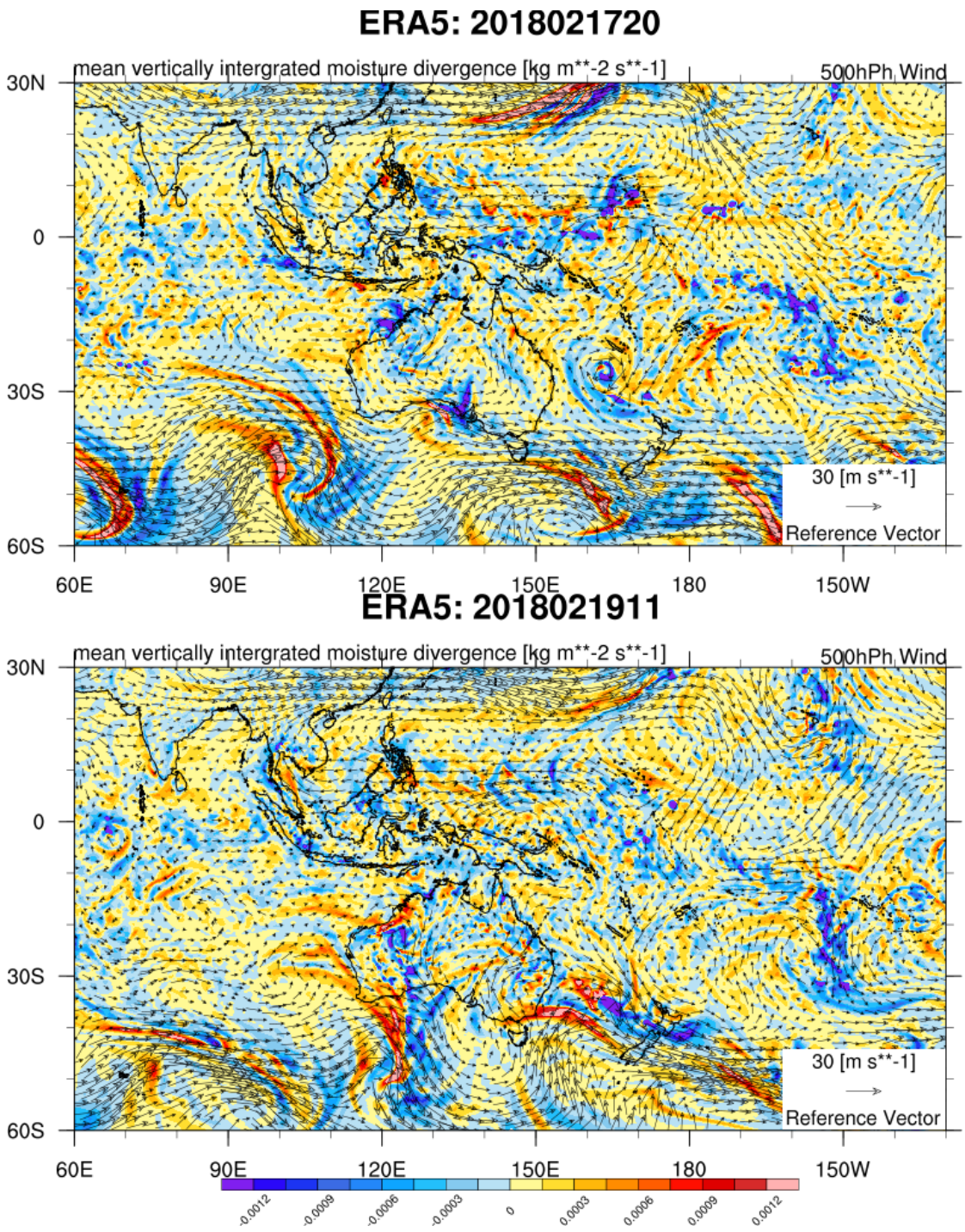

Figure 7. As in Figure 6 but for mean vertically integrated moisture divergence superimposed by 500 hPa wind vectors.

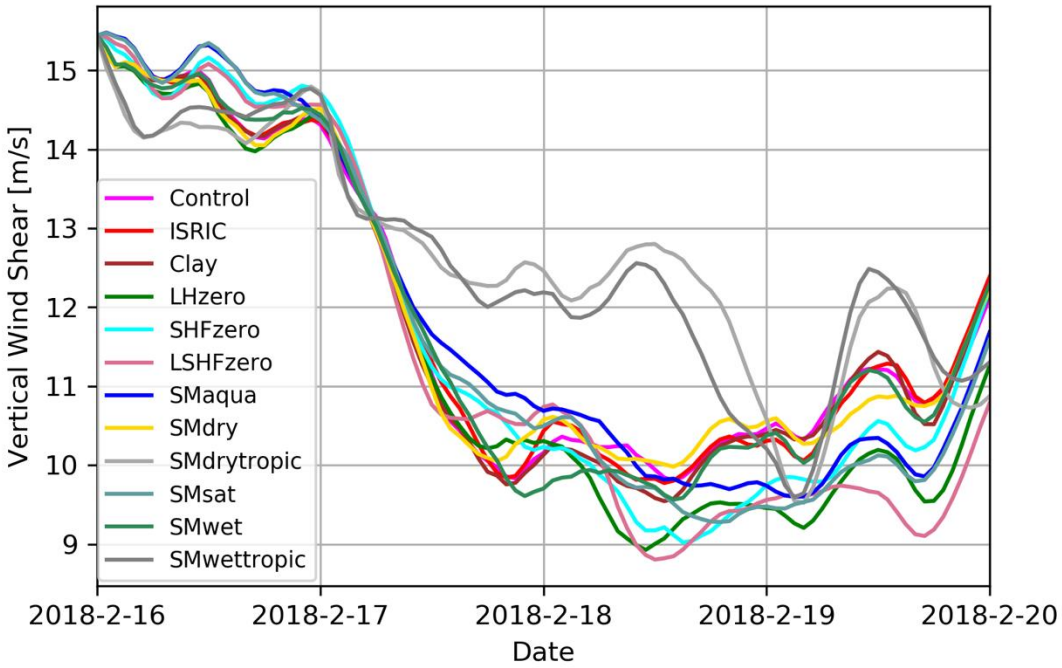

Figure 8. Time series of the areal means of the 850-250 hPa vertical wind shear averaged beyond the radius of 300 km from the center of the simulated storm.

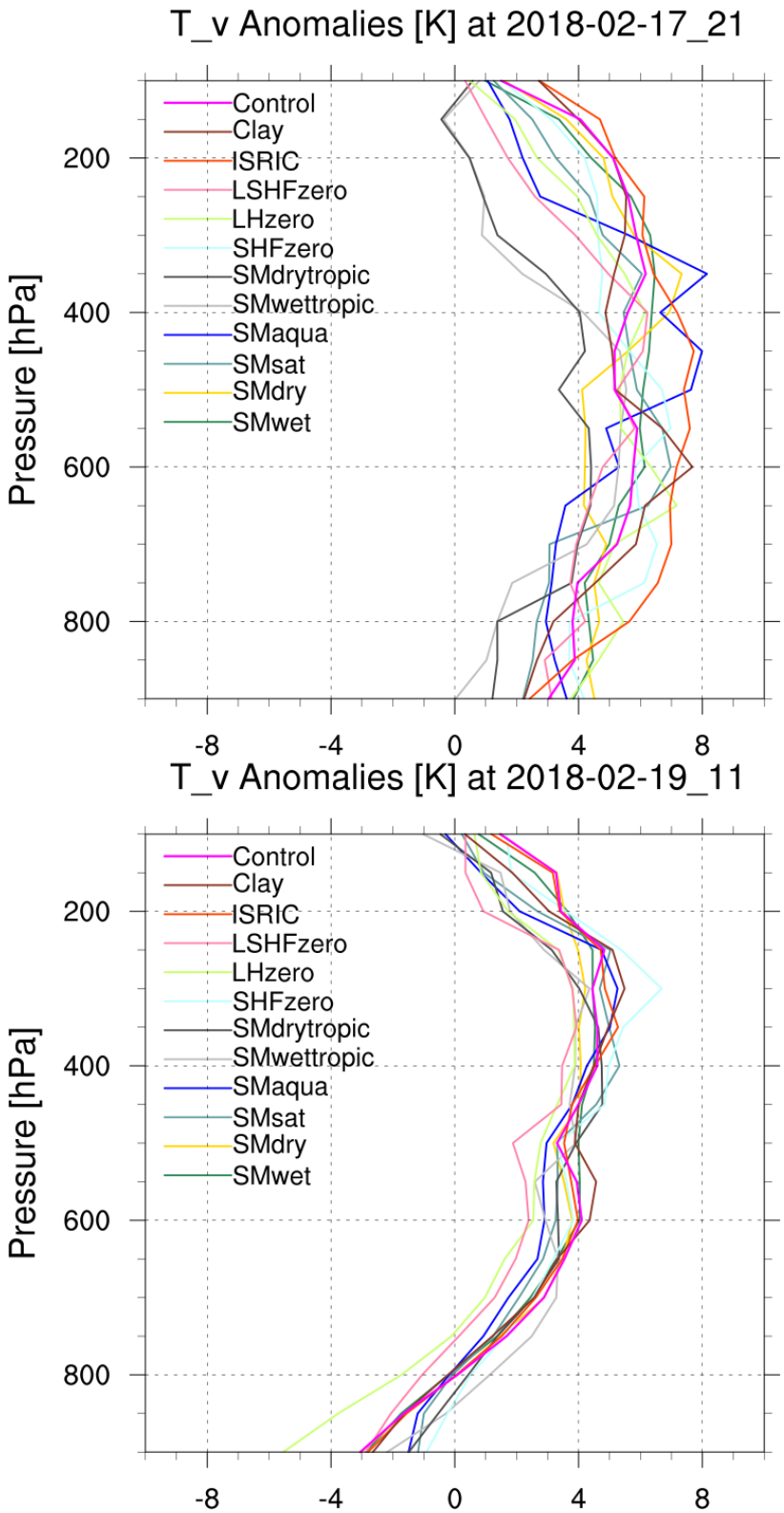

Figure 9. Profiles of virtual temperature anomalies between the eye and the reference environment over a 300-400 km annulus on 17 February at 21 UTC (top) and 19 February at 11 UTC (bottom).

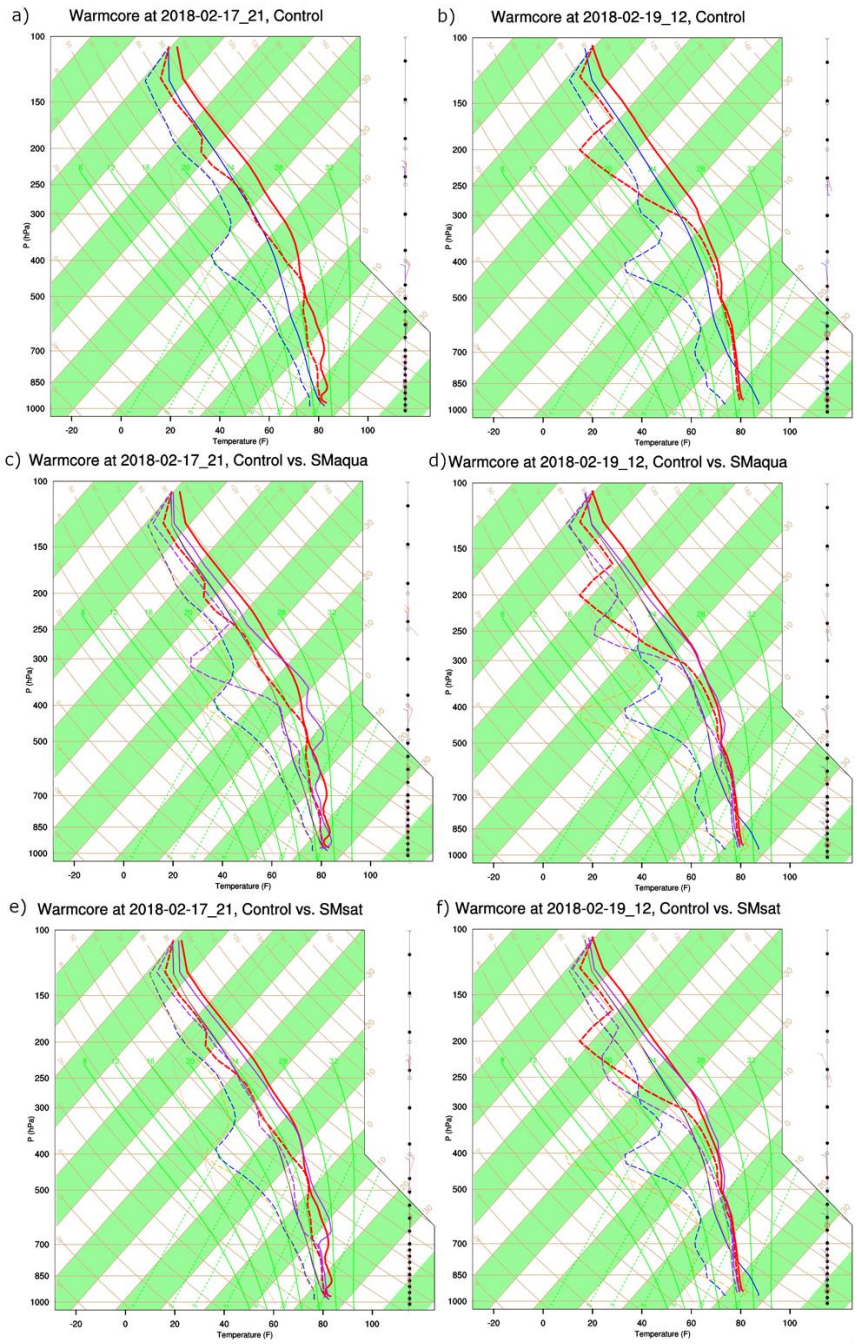

Figure 10. Skew T Log P plots of Control (a and b), SMaqua (c and d), and SMsat (e and f) on 17 February at 21 UTC when the TC Kelvin was intensifying vigorously over ocean (left column) and on 19 February at 12 UTC when the storm was intensifying inland (right column). For Control case, temperature profile at the eye is represented by red line, while temperature profile of the reference environment annular is represented by blue line. Also, dewpoint temperature profile at the eye is represented by red dashed line, while dewpoint temperature profile of the reference environment annular is represented by blue dashed line. For the other cases, likewise, purple and orange colors are used to represent for the eye and the reference environment annular, respectively, along with those for the Control.

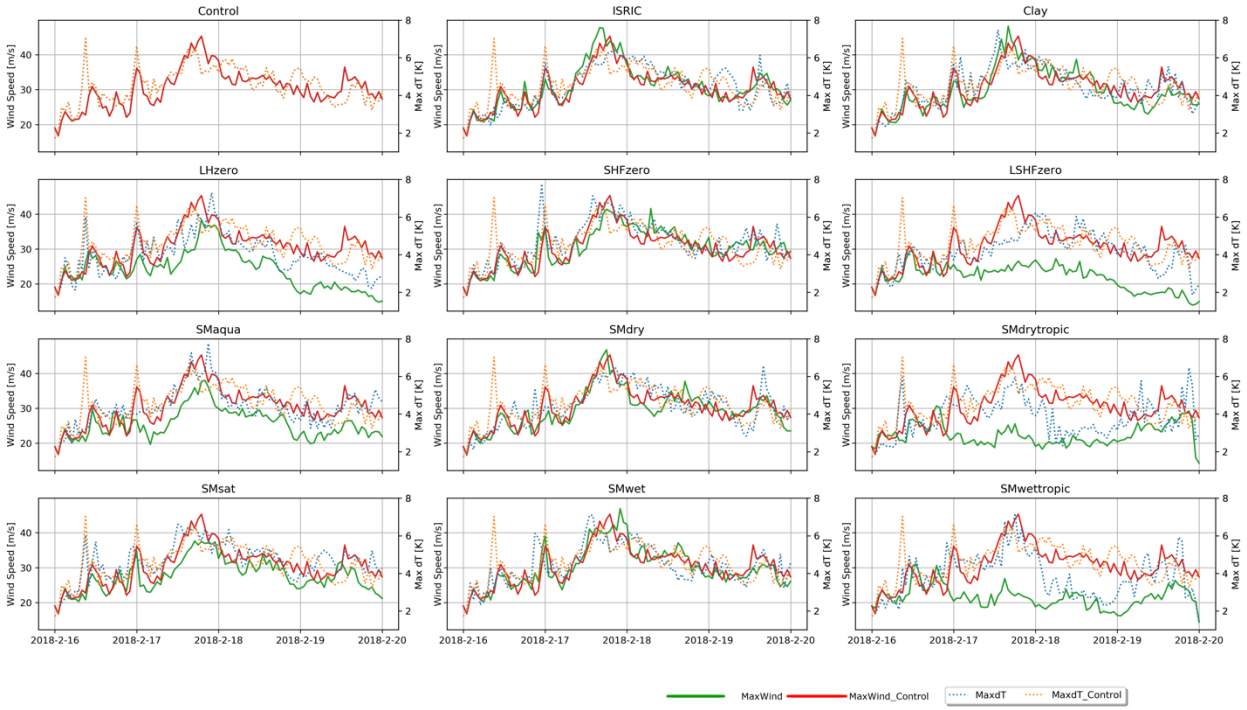

Figure 11. Time series of the maximum of the horizontal temperature differences of the vertical profiles between the warm-core and its environment and the maximum wind speed. Those of the Control case (the red line for wind speed and the dotted orange line for max_dT) are also shown in the other panels for the direct comparisons to those of each case (the green line for wind speed and the dotted blue line for max_dT).

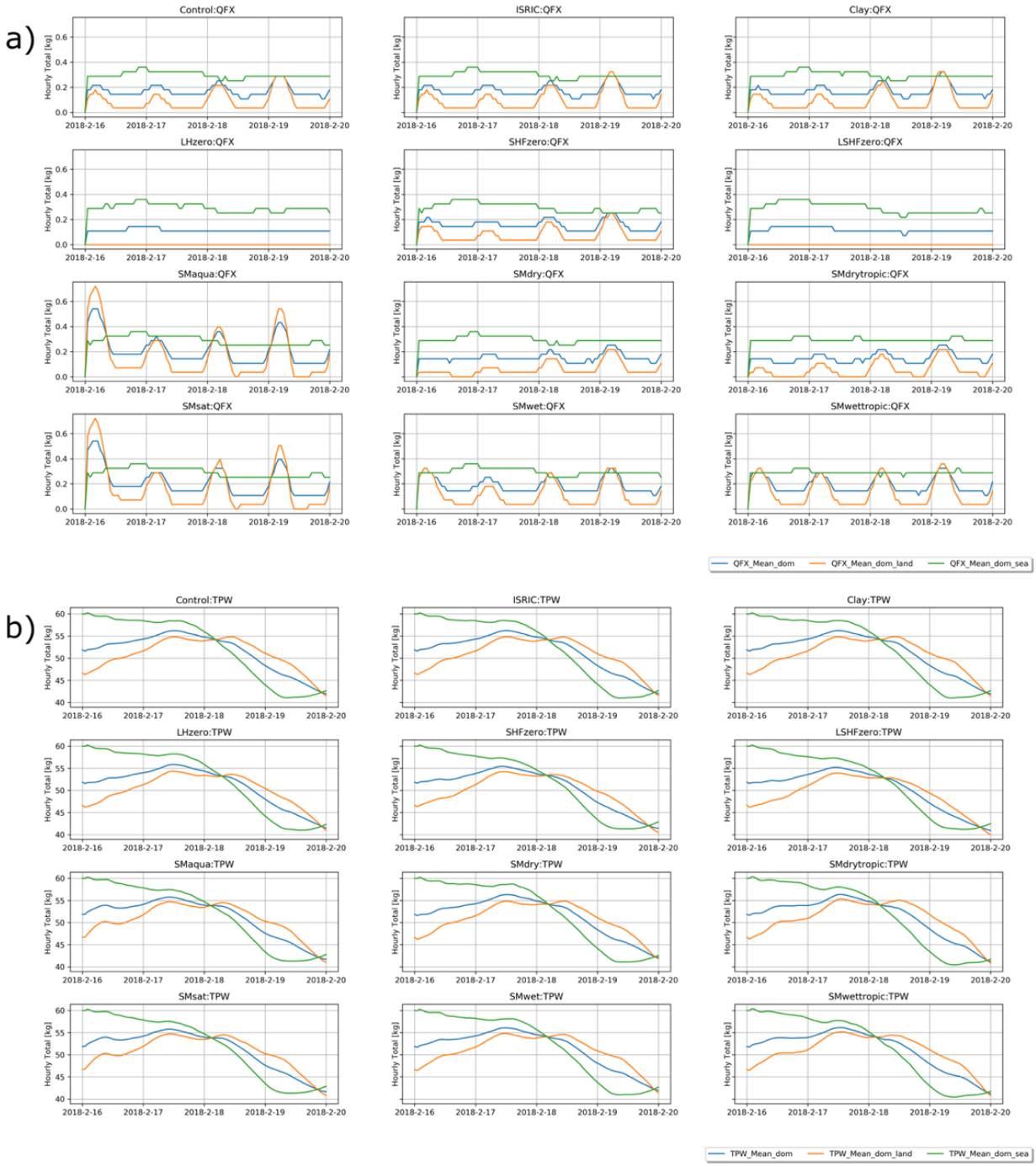

Figure 12. a) Time series of the mean of hourly total moisture fluxes (QFX [kg m^{-2}]) for the entire model domain, land, and sea; b) Time series of Total Precipitable Water (TPW [kg m^{-2}]) that are areal averages of the model entire domain, land, and sea.

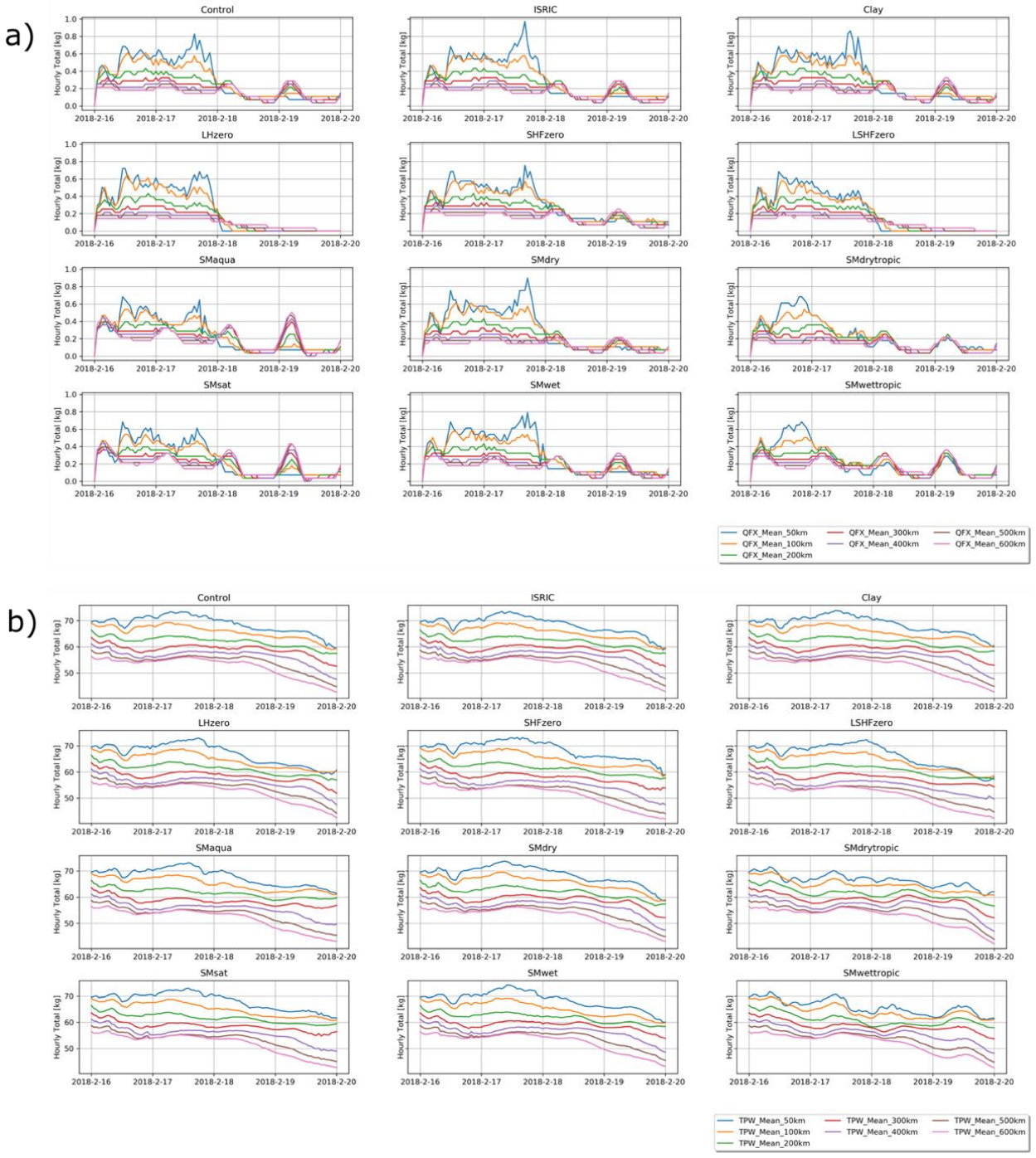

Figure 13. a) Time series of the means of hourly total moisture fluxes (QFX) [kg m^{-2}] averaged within the radii of 50, 100, 200, 300, 400, 500, and 600 km from the center of the simulated storm; b) as in a) but for Total Precipitable Water (TPW [kg m^{-2}]).

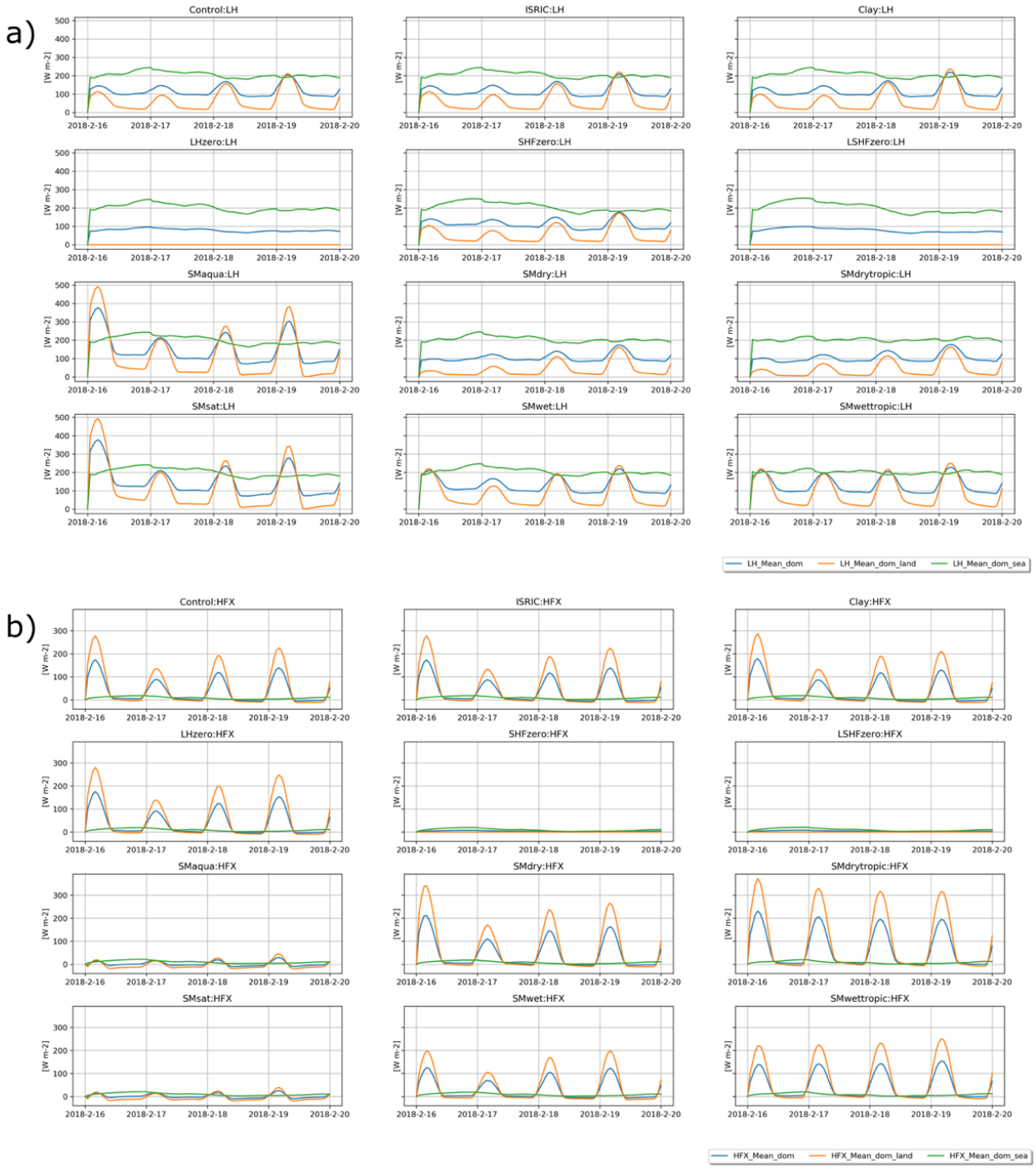

Figure 14. Time series of the mean of a) latent heat fluxes (LH [W m^{-2}]) and b) sensible heat fluxes (SHF [W m^{-2}]) for the entire model domain, land, and sea.

Non-Rendered Figure01

Click here to access/download

Non-Rendered Figure

Fig01.png

Non-Rendered Figure02

Click here to access/download

Non-Rendered Figure

Fig02.png

Non-Rendered Figure03

Click here to access/download

Non-Rendered Figure

Fig03.png

Non-Rendered Figure04

Click here to access/download

Non-Rendered Figure

Fig04.png

Non-Rendered Figure05

Click here to access/download

Non-Rendered Figure

Fig05.png

Non-Rendered Figure06

Click here to access/download

Non-Rendered Figure

Fig06.png

Non-Rendered Figure07

Click here to access/download

Non-Rendered Figure

Fig07.png

Non-Rendered Figure08

Click here to access/download

Non-Rendered Figure

Fig08.png

Non-Rendered Figure09

Click here to access/download

Non-Rendered Figure

Fig09.png

Non-Rendered Figure10

Click here to access/download
Non-Rendered Figure
Fig10.png

Non-Rendered Figure11

Click here to access/download

Non-Rendered Figure

Fig11.png

Click here to access/download

Non-Rendered Figure

Fig12.png

Non-Rendered Figure13

Click here to access/download

Non-Rendered Figure

Fig13.png

Non-Rendered Figure14

Click here to access/download

Non-Rendered Figure

Fig14.png